

# Computational Analysis of Bubble-Structure Interactions in Near-Field Underwater Explosion

Wentao Ma<sup>a</sup>, Xuning Zhao<sup>a</sup>, Christine Gilbert<sup>a</sup>, Kevin Wang<sup>a,\*</sup>

<sup>a</sup>*Department of Aerospace and Ocean Engineering, Virginia Polytechnic Institute and State University, Blacksburg, Virginia 24061, USA*

---

## Abstract

The response of underwater structures to a near-field explosion is coupled with the dynamics of the explosion bubble and the surrounding water. This multiphase fluid-structure interaction process is investigated in the paper using a two-dimensional model problem that features the yielding and collapse of a thin-walled aluminum cylinder. A recently developed computational framework that couples a finite volume compressible fluid dynamics solver with a finite element structural dynamics solver is employed. The fluid-structure and liquid-gas interfaces are tracked using embedded boundary and level set methods. The conservation of mass and momentum across the interfaces is enforced by solving one-dimensional bimaterial Riemann problems. The initial pressure inside the explosion bubble is varied by two orders of magnitude in different test cases. Three different modes of collapse are discovered, including an horizontal collapse (i.e. with one lobe extending towards the explosive charge) that appears counterintuitive, yet has been observed in previous laboratory experiments. Because of the transition of modes, the time it takes for the structure to reach self-contact does not decrease monotonically as the explosion magnitude increases. The fluid pressure and velocity fields, the bubble dynamics, and the transient structural deformation are visualized to elucidate the cause of each collapse mode and the mode transitions. The result suggests that, in addition to the

---

\*Corresponding author  
Email address: kevinwgy@vt.edu (Kevin Wang)

incident shock wave, the second pressure pulse resulting from the contraction of the explosion bubble also has significant effect on the structure's collapse. The phase difference between the structural vibration and the bubble's expansion and contraction influences the structure's mode of collapse. Furthermore, the transient structural deformation has clear effect on the bubble dynamics, leading to a two-way interaction. A counter-jet that points away from the structural surface is observed. Compared to the liquid jets produced by bubbles collapsing near a rigid wall, this counter-jet is in the opposite direction.

*Keywords:* fluid-structure interaction, collapse, bubble dynamics, shock wave, underwater explosion, simulation

---

## 1. Introduction

Underwater explosions pose a significant threat to the structural integrity of marine vehicles, pipelines, and platforms. Accurate prediction of a structure's response to an underwater explosion event is crucial to ensuring safety while reducing the costs associated with overconservative design requirements. If the explosion occurs at a long distance from the structure (i.e. far-field explosion), the load on the structure is dominated by the incident shock wave, which can be captured using one-dimensional hydrodynamics models [1, 2, 3, 4]. If the explosion occurs near the structure (i.e. near-field explosion), the problem becomes more complicated, as the bubble formed by the gaseous explosion products expands and contracts rapidly near the structure. Previous studies have demonstrated that the bubble dynamics, the dynamics of the surrounding liquid water, and the transient deformation of the structure depend on each other, leading to a fluid-structure interaction (FSI) process that involves a multiphase flow, shock waves, complex bubble geometry, large structural deformation, and nonlinear material behaviors (e.g., yielding, fracture) [5, 6, 7, 8, 9, 10].

For thin-walled underwater structures, a primary failure mechanism is instability in the form of collapse. In the past, extensive research efforts have been devoted towards understanding the collapse of cylindrical shell structures

20 (e.g., underwater pipelines, deep-sea submersibles) due to high hydrostatic pressure [11, 12, 13, 14, 15]. In comparison, knowledge about the response of this type of structures to a near-field explosion is still far from complete. A few recent studies suggest that the pulsation of the explosion bubble may have a substantial effect on the structure’s collapse. For example, Gupta *et al.* conducted laboratory experiments on the collapse of aluminum 6061-T6 tubes in a confined environment, in which the tubes are subjected to the combined loading from a prescribed hydrostatic pressure and an explosion that strikes the tubes in the longitudinal direction [6]. Their measurement shows that the magnitude of the first bubble pulse — that is, the increase of pressure due to the first contraction of the explosion bubble — is lower than the incident shock wave, but not negligible. When the hydrostatic pressure is relatively low, the tube starts collapsing after the impact of this bubble pulse, which arrives much later than the incident shock wave. Later, Guzas *et al.* confirmed these findings using fluid-structure coupled simulations [8]. They also showed that the structural collapse may initiate after two to four cycles of bubble expansion and contraction, depending on the hydrostatic pressure. Ikeda conducted implosion experiments using the same type of aluminum tubes within a large pressure chamber, in which the tubes are subjected to a side-on explosion [5]. In these experiments, the initiation of structural collapse also occurs after the arrival of the first bubble pulse. The tubes collapse in mode 2 as expected. But surprisingly, the two lobes are aligned with the loading direction. In other words, the closest point on the cylinder to the explosive charge moves towards the charge. It is hypothesized that this counterintuitive phenomenon is related to the pulsation of the explosion bubble. Although the papers reviewed above (i.e. [6, 8, 5]) do not include details on the explosion bubble dynamics, the results presented therein indicate that the frequency of the bubble’s pulsation can be similar to the first few vibration frequencies of the structure. Moreover, some other studies suggest that the dynamics of a bubble pulsating near a deformable surface can be significantly different from that of the same bubble near a rigid wall, which indicates a two-way interaction between the bubble and the structure. For example, Cao *et*

25  
30  
35  
40  
45  
50

*al.* investigated shock-induced bubble collapse near different types of solid and soft materials, showing that the material’s acoustic impedance has an obvious effect [16]. Several previous studies (e.g., [17, 18, 19, 20, 21]) have investigated bubbles pulsating near a deformable boundary, showing a liquid jet that forms in  
55 a direction away from the boundary, that is, in the opposite direction compared to the jets formed by bubbles near a rigid wall.

In this work, we investigate the response of an underwater, thin-walled aluminum cylinder to a near-field explosion, focusing on the interaction between the pulsation of the explosion bubble and the deformation and collapse of the  
60 cylinder. Clearly, the magnitude of the explosion is a key parameter. A specific objective in this study is to sweep this parameter through a broad range bounded by two extreme values: a low magnitude that does not trigger the collapse of the cylinder, and a high magnitude that causes the cylinder to collapse immediately upon the arrival of the incident shock wave. Based on the research  
65 findings mentioned above, we expect to discover transitions between different types of structural and bubble behaviors.

A recently developed fluid-structure coupled computational framework is employed in this study [22, 23, 24, 25, 26]. The framework couples a finite volume compressible fluid dynamics solver with a nonlinear finite element structural  
70 dynamics solver using a partitioned time-integration procedure [27]. An embedded boundary method is utilized to track the wetted surface of the structure (i.e. the fluid-structure interface), which is capable of handling large structural deformation and topological changes [28, 22]. A level set method is utilized to track the bubble surface (i.e. the liquid-gas interface) [29, 25]. The fluid-  
75 structure and liquid-gas interface conditions are enforced by the FInite Volume method with Exact two-material Riemann problems (FIVER), which naturally accommodates the propagation of shock waves across the interfaces [23, 24, 25]. This computational framework has been verified and validated for several multiphase flow and FSI problems that are closely related to the current applica-  
80 tion [23, 13, 25, 30, 31, 16, 32]. For example, Farhat *et al.* simulated the collapse of aluminum 6061-T6 tubes in modes 2 and 4 due to hydrostatic pressure [13].

They showed that the simulation result is in close agreement with the experimental data in both the transient structural deformation and the pressure pulse generated by the structure’s self-contact. Cao *et al.* simulated the collapse of a bubble in free field and near different solid and soft materials [16]. They showed that the simulated bubble dynamics in free field matches closely the experimental data, and the pressure time-history obtained from a bubble collapsing near a rigid wall agrees well with earlier simulations conducted using a different solver.

In this work, we consider aluminum 6061-T6 as the structural material. To properly account for geometric and material nonlinearities, the computational structural model is based on Green-Lagrange strain tensor and the  $J_2$  flow theory with isotropic hardening. The elastic and plastic properties of the aluminum material are set to be the same as in the validation study presented in Farhat *et al.* [13]. To capture the progressive yielding through the wall of the aluminum cylinder, we resolve the wall thickness explicitly in the finite element mesh. We analyze a two-dimensional model that contains one cross section of the cylinder. This geometric simplification is adopted in many studies on cylinder instabilities (e.g., [33, 34, 35, 36]). In this work, it allows us to perform the aforementioned parameter sweep with mesh convergence at reasonable computational cost. The detonation process is not simulated explicitly. Instead, we initiate the simulations with a small bubble that models the state of the explosion bubble at the end of the detonation process. By varying the pressure (and hence, enthalpy) inside this bubble, we model explosions of different magnitudes. For each simulation, we visualize the fluid pressure and velocity fields, the bubble dynamics, and the transient deformation of the structure. Results from different test cases are contrasted to investigate the impact of the explosion magnitude on the dynamics of the structure and the bubble.

The remainder of this paper is organized as follows. Section 2 presents the physical models and numerical methods employed in this work, and the setup of our simulations. Section 3 presents a mesh convergence analysis that allowed us to determine the mesh resolution for this study. It also shows that upon convergence, the mode of collapse reported in Ikeda [5] is replicated. In Section 4,

we present five representative test cases with different initial pressures inside the bubble, which led to drastically different structural behaviors ranging from cyclic elastic vibration to an immediate collapse without vibration. In Section 5, we categorize the different collapse behaviors observed in the parametric study into three modes, and discuss the cause of each mode as well as the mechanisms underlying the mode transitions. Finally, a few concluding remarks are provided in Section 6.

## 2. Physical models and numerical methods

### 2.1. Physical models

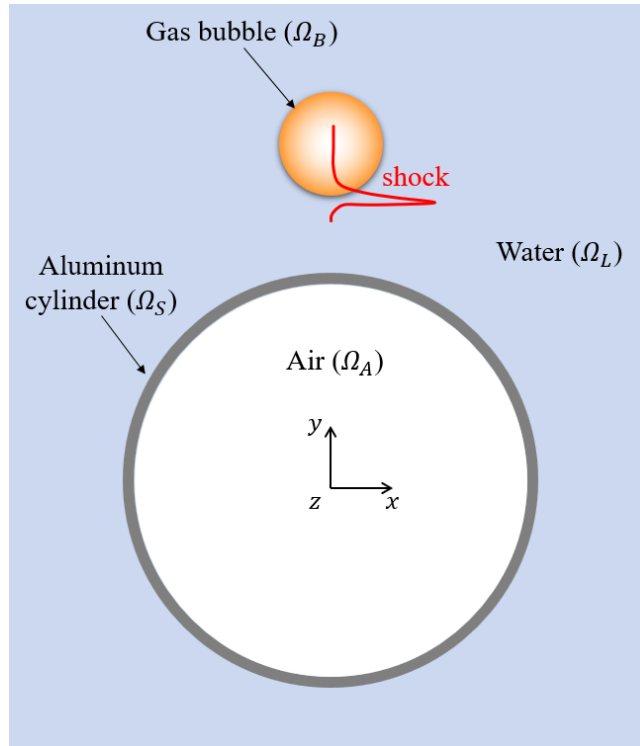


Figure 1: A two-dimensional model of an underwater aluminum cylinder subjected to a near-field explosion. (The  $z$  axis is aligned with the longitudinal direction of the cylinder.)

Figure 1 presents an illustration of the problem investigated in this work. A thin-walled, air-filled circular cylinder is submerged in water. An underwater

explosion occurs in the close proximity of the cylinder, and is modeled as a gas  
125 bubble with high internal pressure and density. Let  $\Omega_S$ ,  $\Omega_L$ ,  $\Omega_A$ , and  $\Omega_B$  denote  
the subdomains occupied by the aluminum material, the liquid water, the air  
inside the cylinder, and the gas bubble, respectively. The multiphase fluid flow  
is dominated by shock waves and high pressure. In comparison, viscous stresses  
and heat diffusion can be neglected. Therefore, the following Euler equations  
130 are solved in  $\Omega_L$ ,  $\Omega_A$ , and  $\Omega_B$ .

$$\frac{\partial \mathbf{W}(x, t)}{\partial t} + \nabla \cdot \mathcal{F}(\mathbf{W}) = \mathbf{0}, \quad \forall \mathbf{x} \in \Omega_L(t) \cup \Omega_A(t) \cup \Omega_B(t), \quad t > 0, \quad (1)$$

with

$$\mathbf{W} = \begin{bmatrix} \rho \\ \rho \mathbf{V} \\ \rho e_t \end{bmatrix}, \quad \mathcal{F} = \begin{bmatrix} \rho \mathbf{V}^T \\ \rho \mathbf{V} \otimes \mathbf{V} + p \mathbf{I} \\ (\rho e_t + p) \mathbf{V}^T \end{bmatrix}. \quad (2)$$

Here,  $\rho$ ,  $e_t$ , and  $p$  denote the mass density, total energy per unit mass, and  
pressure, respectively.  $\mathbf{V}$  is the velocity vector.  $\mathbf{I}$  denotes the the  $3 \times 3$  identity  
matrix.

$$e_t = e + \frac{1}{2} |\mathbf{V}|^2, \quad (3)$$

135 where  $e$  is the internal energy per unit mass.

Equation (1) is closed by an equation of state (EOS) for each fluid material.  
For the gas inside the bubble and the air inside the cylinder, we apply the perfect  
gas EOS, i.e.

$$p = (\gamma - 1) \rho e, \quad (4)$$

where  $\gamma$  is the heat capacity ratio. For the liquid water, we apply the Tait EOS,

$$140 \quad p = p_c + \alpha \left( \left( \frac{\rho}{\rho_c} \right)^\beta - 1 \right), \quad (5)$$

where  $\alpha = 3.5291 \times 10^8$  Pa and  $\beta = 6.4762$  [22].  $(\rho_c, p_c)$  is a reference state,  
which is set by  $\rho_c = 1.0 \times 10^3$  kg/m<sup>3</sup> and  $p_c = 1.0 \times 10^5$  Pa in this work. For  
each equation of state  $p(\rho, e)$ , the speed of sound,  $c$ , is given by

$$c = \sqrt{\left. \frac{\partial p}{\partial \rho} \right|_e + \frac{p}{\rho^2} \left. \frac{\partial p}{\partial e} \right|_\rho}. \quad (6)$$

Within the solid subdomain,  $\Omega_S$ , the dynamic equilibrium of the cylinder  
 145 undergoing finite deformation is modeled in the Lagrangian setting [37], i.e.

$$\rho_s \ddot{\mathbf{u}}(\mathbf{X}, t) - \nabla \cdot (J^{-1} \mathbf{F} \cdot \mathbf{S} \cdot \mathbf{F}^T) = \mathbf{b}, \quad \forall \mathbf{X} \in \Omega_S(0), \quad t > 0. \quad (7)$$

Here,  $\rho_s$  denotes the solid material's density,  $\mathbf{u}$  the displacement vector,  $\mathbf{X}$   
 the material coordinates,  $\mathbf{S}$  the second Piola-Kirchhoff stress tensor,  $\mathbf{F}$  the  
 deformation gradient, and  $J = \det \mathbf{F}$ .  $\mathbf{b}$  is the body force vector acting on the  
 cylinder, which is assumed to be zero in this study. The dots above  $\mathbf{u}$  indicate  
 150 its partial derivative with respect to time.

The cylinder is assumed to be made of aluminum alloy 6061-T6, and can  
 undergo yielding and plastic deformation. Following Farhat *et al.* [13], it is  
 modeled as an elastic-plastic material, using the  $J_2$  flow theory with isotropic  
 hardening. The yield criterion is defined by

$$\sqrt{2J_2(\mathbf{s})} = \left( \frac{3}{2} \mathbf{s} \cdot \mathbf{s} \right)^{1/2} = \sigma_e, \quad (8)$$

155 where  $\mathbf{s}$  is the deviator of the second Piola-Kirchhoff stress tensor, and  $\sigma_e$  the  
 von Mises effective stress.

The fluid-structure interface is given by

$$\Gamma_{FS} = \partial\Omega_S(t) \cap (\partial\Omega_L(t) \cup \partial\Omega_A(t) \cup \partial\Omega_B(t)). \quad (9)$$

Across the fluid-structure interface, the normal velocity and the surface trac-  
 tion are continuous, i.e.

$$\begin{aligned} (\mathbf{V} - \dot{\mathbf{u}}) \cdot \mathbf{n} &= 0, \\ -p\mathbf{n} &= \boldsymbol{\sigma} \cdot \mathbf{n}, \end{aligned} \quad \text{on } \Gamma_{FS}, \quad (10)$$

160 where  $\mathbf{n}$  denotes the unit normal to  $\Gamma_{FS}$ ,  $\boldsymbol{\sigma}$  the Cauchy stress tensor, which is  
 related to the second Piola-Kirchhoff stress by  $\boldsymbol{\sigma} = J^{-1} \mathbf{F} \cdot \mathbf{S} \cdot \mathbf{F}^T$ .

The bubble surface (i.e. liquid-gas interface) is given by

$$\Gamma_{FF} = \partial\Omega_L(t) \cap \partial\Omega_B(t). \quad (11)$$

We assume that the two fluid materials across  $\Gamma_{FF}$  are immiscible. In addition,  
 surface tension is negligible compared to the hydrodynamic pressure. Therefore,



165 normal velocity and pressure are assumed to be continuous across  $\Gamma_{FF}$ , i.e.

$$\left( \lim_{\mathbf{x}' \rightarrow \mathbf{x}, \mathbf{x}' \in \Omega_L} \mathbf{V}(\mathbf{x}') - \lim_{\mathbf{x}' \rightarrow \mathbf{x}, \mathbf{x}' \in \Omega_B} \mathbf{V}(\mathbf{x}') \right) \cdot \mathbf{n} = 0, \quad \forall \mathbf{x} \in \Gamma_{FF}. \quad (12)$$

$$\lim_{\mathbf{x}' \rightarrow \mathbf{x}, \mathbf{x}' \in \Omega_L} p(\mathbf{x}') = \lim_{\mathbf{x}' \rightarrow \mathbf{x}, \mathbf{x}' \in \Omega_B} p(\mathbf{x}')$$

To track the evolution of the liquid-gas interface, we solve the level-set equation,

$$\frac{\partial \phi(\mathbf{x}, t)}{\partial t} + \mathbf{V} \cdot \nabla \phi = 0, \quad \forall \mathbf{x} \in \Omega_L \cup \Omega_A \cup \Omega_B \cup \Omega_S, \quad (13)$$

where  $\phi(\mathbf{x}, t)$  denotes the level set function, initialized to be the signed shortest distance from  $\mathbf{x}$  to the interface. In this way, the large deformation and topological changes (e.g. splitting and merging) of the bubble surface are accommodated  
170 without the need of any special treatment.

In summary, Figure 2 presents an overview of the model equations solved in this work, as well as their dependencies.

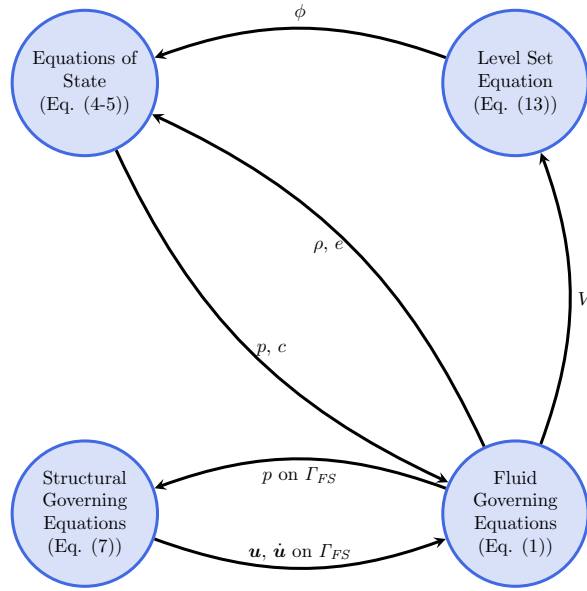


Figure 2: Physical models adopted in this work and their dependencies.

## 2.2. Numerical methods

175 A recently developed multiphase fluid-structure coupled computational framework is applied to solve the aforementioned governing equations [24, 23, 28, 25]. This framework couples a nonlinear finite element solid dynamics solver with a finite volume fluid dynamics solver using a partitioned procedure.

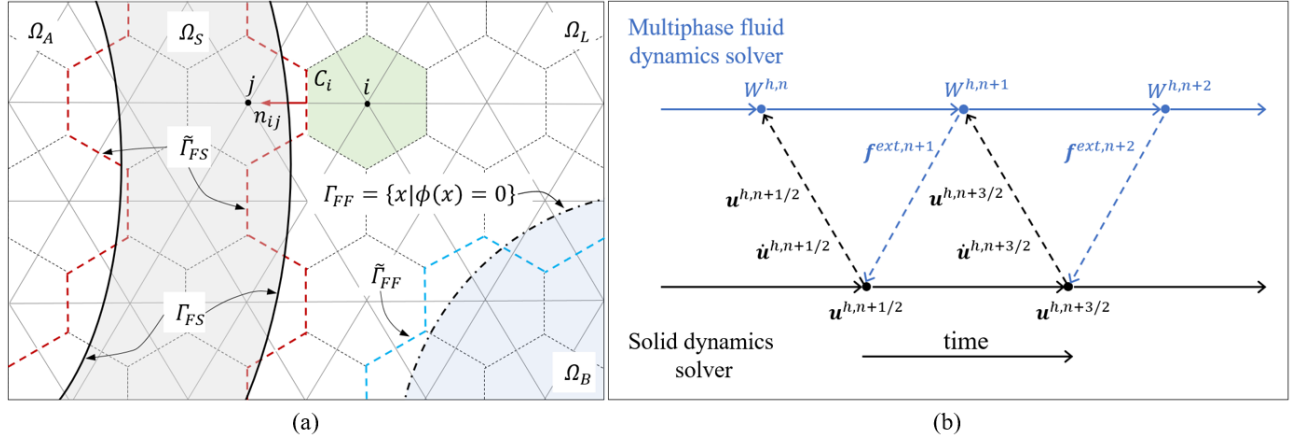


Figure 3: Illustration of the discretization methods in space (a) and time (b).

As shown in Figure 3(a), an augmented fluid domain  $\tilde{\Omega}$  is defined to include  
 180 the space occupied by the liquid, the gas bubble, the cylinder, and the air inside,  
 i.e.

$$\tilde{\Omega} = \Omega_L \cup \Omega_B \cup \Omega_S \cup \Omega_A. \quad (14)$$

In  $\tilde{\Omega}$ , a node-centered, unstructured, and non-interface-conforming finite volume  
 mesh is used to semi-discretize the fluid governing equations. Around each node  
 (e.g. Node  $i$  in Figure 3(a)), a control volume  $C_i$  is constructed. Integrating  
 185 Eq. (1) within  $C_i$  gives the semi-discrete form,

$$\frac{\partial \mathbf{W}_i}{\partial t} + \frac{1}{\|C_i\|} \sum_{j \in N(i)} \int_{\partial C_{ij}} \mathcal{F}(\mathbf{W}) \cdot \mathbf{n}_{ij} dS = 0, \quad (15)$$

where  $\mathbf{W}_i$  denotes the average of  $\mathbf{W}$  in  $C_i$ .  $\|C_i\|$  denotes the volume of  $C_i$ .  
 $N(i)$  is the set of neighboring nodes that are connected to node  $i$  by an edge.  
 $\partial C_{ij} = \partial C_i \cap \partial C_j$  is the interface between  $C_i$  and  $C_j$ .  $\mathbf{n}_{ij}$  is the unit vector

normal to  $\partial C_{ij}$ . We compute the surface integral over  $\partial C_{ij}$  in different ways,  
 190 depending on the location of nodes  $i$  and  $j$  — specifically, which fluid or solid  
 subdomain they belong to. The following four scenarios are considered.

- (1) Nodes  $i$  and  $j$  are both located in the same fluid subdomain ( $\Omega_L$  or  $\Omega_A$  or  
 $\Omega_B$ ). In this case, the method of monotonic upwind scheme conservation  
 law (MUSCL) [38] and Roe’s flux [39] are used to calculate the flux  $\mathcal{F}(\mathbf{W})$   
 195 across  $\partial C_{ij}$ .
- (2) Nodes  $i$  and  $j$  belong to different fluid subdomains. In this scenario, a  
 one-dimensional (1-D) two-fluid Riemann problem is constructed along  
 the edge  $i$ - $j$ , that is,

$$\frac{\partial \mathbf{w}}{\partial \tau} + \frac{\partial \mathcal{F}(\mathbf{w})}{\partial \xi} = 0, \quad \text{with } \mathbf{w}(\xi, 0) = \begin{cases} \mathbf{w}_i & \text{if } \xi \leq 0, \\ \mathbf{w}_j & \text{if } \xi > 0, \end{cases} \quad (16)$$

where  $\tau$  denotes the time coordinate, and  $\xi$  the local spatial coordinate  
 200 aligned with  $\mathbf{n}_{ij}$  and centered at the midpoint between  $i$  and  $j$ . The initial  
 states  $\mathbf{w}_i$  and  $\mathbf{w}_j$  are projections of  $\mathbf{W}_i$  and  $\mathbf{W}_j$  on the  $\xi$  axis. This 1-D  
 Riemann problem is solved exactly. Its solution is supplied to Roe’s flux  
 function to calculate the flux across  $\partial C_{ij}$ , thereby enforcing the interface  
 conditions (Eq. (12)) [24].

- (3) One of the two nodes belongs to a fluid subdomain, while the other node  
 205 belongs to the solid subdomain,  $\Omega_S$ . In this case, a 1-D fluid-structure  
 Riemann problem with a moving wall boundary is constructed. For ex-  
 ample, if node  $i$  is the one in a fluid subdomain, the Riemann problem is

$$\frac{\partial \mathbf{w}}{\partial \tau} + \frac{\partial \mathcal{F}(\mathbf{w})}{\partial \xi} = 0, \quad \tau > 0, \quad \xi < v_S \tau, \quad (17)$$

$$\mathbf{w}(\xi, 0) = \mathbf{w}_i, \quad \xi < 0, \quad (18)$$

$$v(v_S \tau, \tau) = v_S, \quad \tau > 0, \quad (19)$$

where  $\xi$  is the local spatial coordinate along  $\mathbf{n}_{ij}$ , centered at the midpoint  
 between  $i$  and  $j$ . The initial state  $\mathbf{w}_i$  is reconstructed by the fluid state  
 $\mathbf{W}_i$ .  $v_S$  denotes the normal velocity of the structure at its intersection

215 with edge  $i - j$ , which is computed by the structural dynamics solver. Similar to the previous scenario, the exact solution of this 1-D Riemann problem is supplied to Roe's flux function to calculate the flux across  $\partial C_{ij}$  [23, 28].

(4) Both nodes  $i$  and  $j$  belong to the solid subdomain. In this case, the flux  
220 across  $\partial C_{ij}$  is set to 0.

The algorithm above is referred to as FIVER, which stands for FInite Volume method with EXact two-material Riemann problems [22, 24, 23, 28, 25, 29, 40, 26]. It has been employed in the past to simulate the collapse of underwater structures due to hydrostatic pressure [13, 41, 9], as well as bubble dynamics in  
225 free field and near different material boundaries [42, 16]. FIVER requires tracking the fluid-structure and liquid-gas interfaces in the non-interface-conforming, unstructured mesh  $\tilde{\Omega}^h$ . A collision-based computational geometry algorithm [22, 28] is applied to track the fluid-solid interface.

The liquid-gas interface is tracked implicitly by solving the level set equation (13). In this study, (13) is first rearranged to obtain  
230

$$\frac{\partial \phi(\mathbf{x}, t)}{\partial t} + \nabla \cdot (\phi \mathbf{V}) = \phi \nabla \cdot \mathbf{V}. \quad (20)$$

Equation (20) is solved using a finite volume method on the same fluid mesh. Specifically, the convection term,  $\nabla \cdot (\phi \mathbf{V})$ , is discretized using the same MUSCL scheme, but without a slope limiter. The term  $\phi \nabla \cdot \mathbf{V}$  on the right-hand-side is treated as a source term. Additional details can be found in [25].

235 A Galerkin finite element method is applied to semi-discretize the weak form of Equation (7), which yields

$$\mathbf{M} \frac{\partial^2 \mathbf{u}^h}{\partial t^2} + \mathbf{f}^{int} \left( \mathbf{u}^h, \frac{\partial \mathbf{u}^h}{\partial t} \right) = \mathbf{f}^{ext}, \quad (21)$$

where  $\mathbf{M}$  denotes the mass matrix,  $\mathbf{u}^h$  denotes the discrete displacement vector;  $\mathbf{f}^{int}$  and  $\mathbf{f}^{ext}$  denote the discrete internal force and external force vector, respectively.

240 The staggered fluid-structure time integrator presented in [27] is used in this work to integrate the coupled fluid and structural governing equations. The fluid

equations are integrated in time using an explicit fourth-order Runge–Kutta method, while the structural equations are integrated using the second-order central difference scheme. Notably, the fluid and solid time steps are offset by half a step (Figure 3(b)). This is a designed feature to achieve second-order accuracy in time while maintaining optimal numerical stability.

### 2.3. Simulation setup

The setup of the numerical simulations is shown in Figure 4, including the dimensions of the cylinder and the bubble. A fluid pressure sensor, P1, is placed in the subdomain of liquid water at a location that is close to both the cylinder and the bubble. Also, three displacement and strain sensors are placed on the inner wall of the cylinder. The material and geometric properties of the cylinder are listed in Table 1. In particular, the aluminum material properties are set to be the same as in [13]. The properties of the bubble are listed in Table 2. Here, the stand-off distance is defined as the shortest distance between the bubble’s center and the cylinder’s outer surface. The bubble’s initial pressure in this study is varied from 1.0 MPa to 100.0 MPa in different test cases. The properties of the ambient water and the air inside the cylinder are listed in Table 3.

Table 1: Material and geometric properties of the cylinder (Aluminum 6061-T6)

Young’s modulus	Poisson’s ratio	Density	Yield stress	Tangent modulus	Outer diameter	Thickness
69.6 GPa	0.33	2779 kg/m <sup>3</sup>	292 MPa	674 MPa	38.911 mm	0.711 mm

Table 2: Bubble properties

Stand-off distance	Initial radius	Initial density	Initial pressure	Heat capacity ratio
10.189 mm	2.5 mm	50.0 kg/m <sup>3</sup>	1.0 to 100.0 MPa	1.4



270 is a square with a length of 1,200 mm, which is approximately 30 times the  
diameter of the structure. Figure 5(b) highlights the fact that the fluid mesh  
does not conform to the boundary of the structure. The embedded boundary  
method described in Section 2.2 is employed to track the structure within this  
fluid mesh.

275 All the computations are performed using the Tinkercliffs computer cluster  
at Virginia Tech. The fluid dynamics solver is parallelized using Message Passing  
Interface (MPI). As an example, for mesh pair 8, the fluid mesh is divided into  
2,047 subdomains, each one assigned to an AMD EPYC 7702 processor core.  
The time step size is  $3.5 \times 10^{-6}$  ms. To advance the physical time by 1.0 ms,  
280 28.3 hours of wall-clock time are needed, which means a computational cost of  
 $5.8 \times 10^4$  core-hours. The total computational cost of the simulation on mesh  
pair 8 is  $2.3 \times 10^5$  core-hours.

Table 4: Fluid and structural meshes used in the mesh convergence analysis.

	Structural Mesh		Fluid Mesh	
	Resolution*	Num. of Nodes	Element Size** (mm)	
Pair 1	$100 \times 1$	$4.29 \times 10^4$	1.2	
Pair 2	$200 \times 3$	$1.71 \times 10^5$	0.6	
Pair 3	$260 \times 4$	$2.99 \times 10^5$	0.45	
Pair 4	$336 \times 4$	$4.66 \times 10^5$	0.36	
Pair 5	$400 \times 5$	$6.74 \times 10^5$	0.3	
Pair 6	$600 \times 5$	$6.74 \times 10^5$	0.3	
Pair 7	$600 \times 5$	$1.51 \times 10^6$	0.2	
Pair 8	$1000 \times 10$	$4.19 \times 10^6$	0.12	

\* The first/second number is the number of elements to resolve the circumference/thickness of the cylinder.

\*\* In the most refined region.

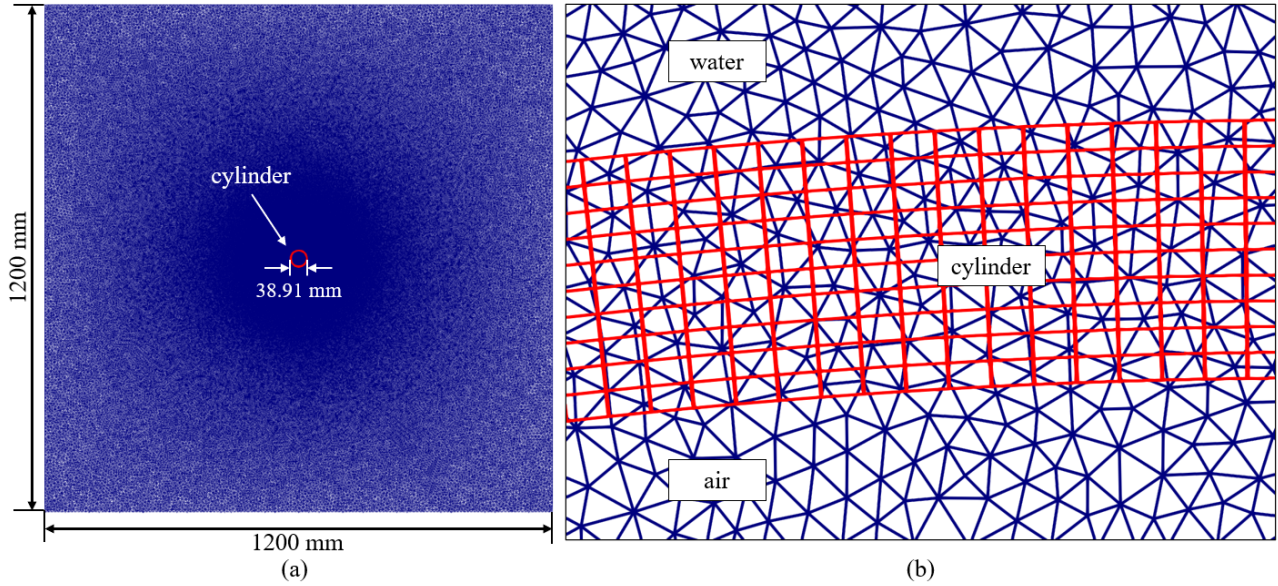


Figure 5: Example fluid and structural meshes (Pair 8): the entire computational domain (a) and a zoom-in snapshot around the fluid-structure interface (b).

Figure 6 presents four solution snapshots obtained using the finest meshes (i.e. Pair 8). As soon as the simulation begins, the bubble generates a strong outgoing shock wave because of the high internal pressure. The first snapshot (285  $t = 0.022$  ms) captures the impact of this shock wave on the cylinder as well as the reflection. At the same time, the bubble starts to expand, which can be observed from the fluid velocity field. The second snapshot ( $t = 0.706$  ms) is taken at a time shortly after the bubble reaches its maximum size. The third snapshot (290  $t = 3.259$  ms) is taken after the bubble has gone through two cycles of oscillation (i.e. expansion and contraction). A liquid jet, which points away from the structure, penetrates the bubble's top surface. At this time instant, the structure has lost stability and undergone large deformation. Consequently, plastic strain occurs on the structure. It can be observed in the top image of 295 Figure 6(c) that plastic deformation is concentrated at the left, right, top, and bottom portions of the cylinder. The last snapshot is taken at  $t = 3.864$  ms, shortly after the structure has reached self-contact. The emission of a shock



wave at the point of contact can be clearly observed. This type of *implosion* shock waves have been observed and investigated in the past in the context of hydrostatic collapse [13, 43, 44, 45]. Notably, in the final configuration, the two lobes of the structure extends in the vertical direction, that is, in the propagation direction of the incident shock wave. The same behavior has been observed in a previous laboratory experiment reported in Ikeda [5](Figure 7). The cause of this mode of collapse will be discussed in Section 4 of this paper.

Figure 8 shows the convergence of the numerical results as the mesh gets refined. Two quantities of interest are examined, namely the structural displacement at the sensor location marked in Figure 6, and the bubble size. Both of them are measured at  $t = 3.259$  ms. As the mesh gets refined, the convergence of these quantities are achieved. From mesh pairs 4 to 8, although the computational cost is increased by 30 times (in terms of core-hours), the result only changes 18.8% in sensor displacement and 12.2% in bubble size. Based on this analysis, mesh pair 6 is selected for the parametric study in the subsequent sections of the paper. The discrepancy between the solution obtained using mesh pair 6 and that using mesh pair 8 is only 0.76% in sensor displacement and 3.71% in bubble size.

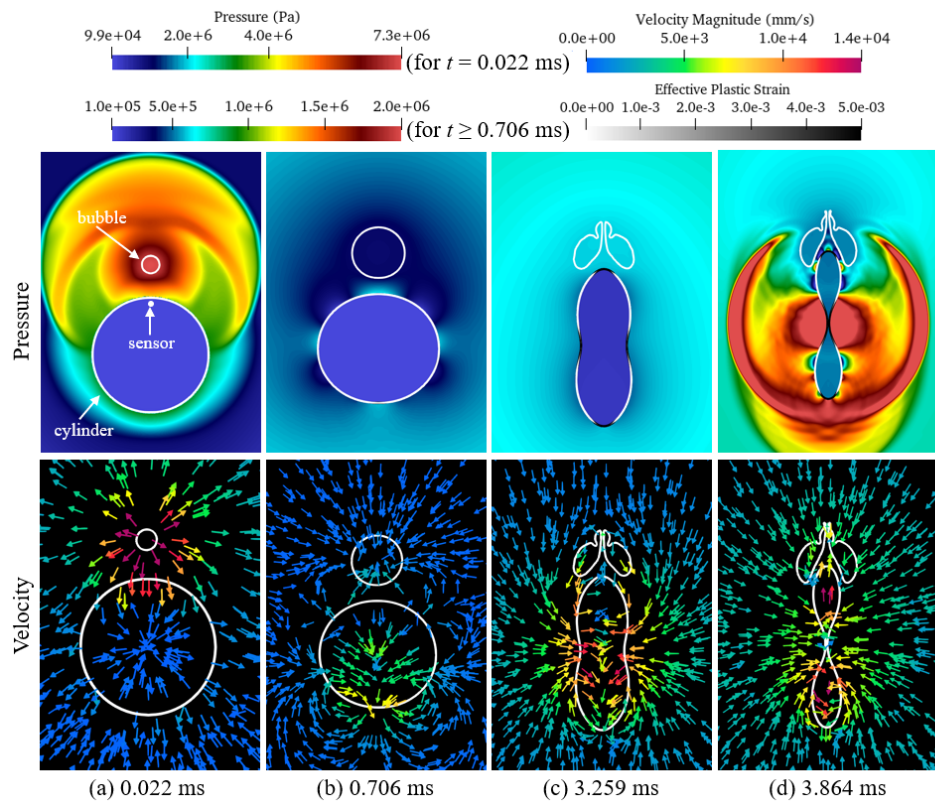


Figure 6: Results obtained using mesh pair 8 at four different time instants: The fluid pressure field and the plastic deformation of the structure (top row), and the fluid velocity field (bottom row).

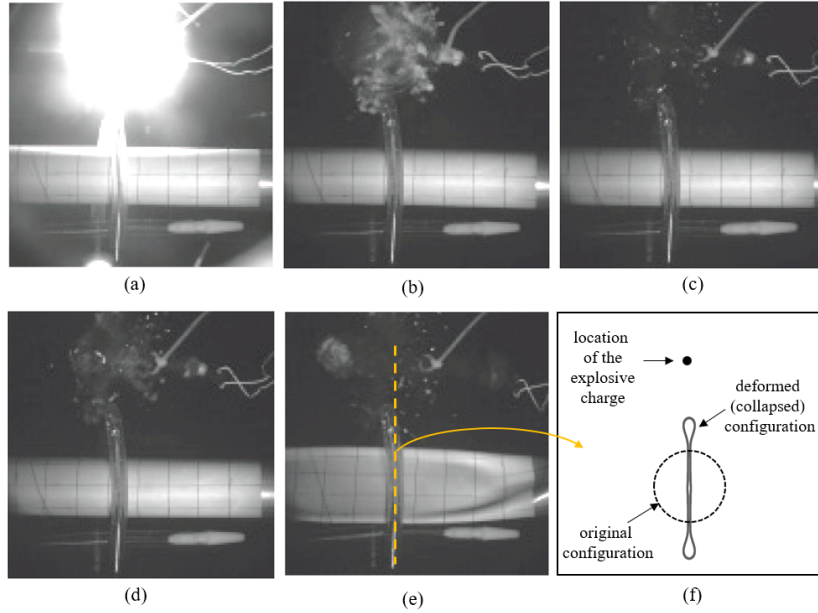


Figure 7: Experimental result of the collapse of an aluminum 6061 tube due to a near-field explosion (Ikeda [5], test AE05r01). (a)-(e) A sequence of images from the high-speed movie obtained from this test. (f) Schematic drawing of the collapsed cylinder (a cross-sectional view).

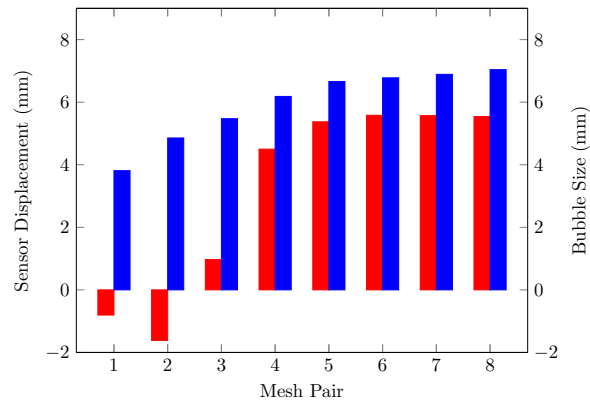


Figure 8: Mesh convergence analysis: Vertical displacement at the sensor marked in Figure 6 (red) and bubble size (radius equivalent, blue) at 3.259 ms, obtained using different pairs of meshes. (Pair 1: coarsest, Pair 8: finest)

#### 4. Bubble-structure interaction and different collapse modes

To elucidate the dynamic bubble-fluid-structure interaction and the impact of this interaction on the structure’s collapse, a parametric study was conducted with initial pressure inside the bubble (denoted by  $p_0$ ) varied from 1 MPa to 100 MPa in different test cases, while all other parameters remained fixed. It was observed that the dynamics of the bubble and the structure do not evolve monotonically with respect to the variation of  $p_0$ . In this section, we present five (5) representative cases that exhibit dramatically different modes, whereas the transition among these modes is discussed in Section 5.

##### 4.1. $p_0 = 8.0$ MPa (enthalpy: 0.5498 J/mm)

In this case, the pressure load created by the bubble is not high enough to make the cylinder collapse. The dynamic process features the cyclic expansion and contraction of the bubble, coupled with the oscillation of the cylinder. Figure 9 presents a series of solution snapshots that show the evolution of the bubble, the cylinder, and the fluid pressure and velocity fields. Furthermore, the structural deformation is characterized by the distance between the cylinder’s top and bottom points and the distance between its left and right points, as shown in Figure 10(a). The time histories of bubble size and fluid pressure at a sensor location (P1 in Figure 4) are shown in Figure 10(b).

In Figure 9, the first snapshot (sub-figure ①) is taken at  $t = 0.022$  ms, shortly after the incident shock wave generated by the bubble reaches the surface of the cylinder. The bubble is impacted by the reflection of the incident shock wave against the cylinder, which is the first evidence of a two-way coupling between bubble and structural dynamics. The expanding bubble pushes the surrounding water. Therefore, the top portion of the cylinder is impacted by both a pressure load from the incident shock wave and a momentum from the water flow. As a result, the cylinder is compressed vertically. Around  $t = 0.470$  ms (Figure 9 ②), the bubble is about to reach its maximum size. As the speed of its expansion decreases, the pressure of the surrounding water also

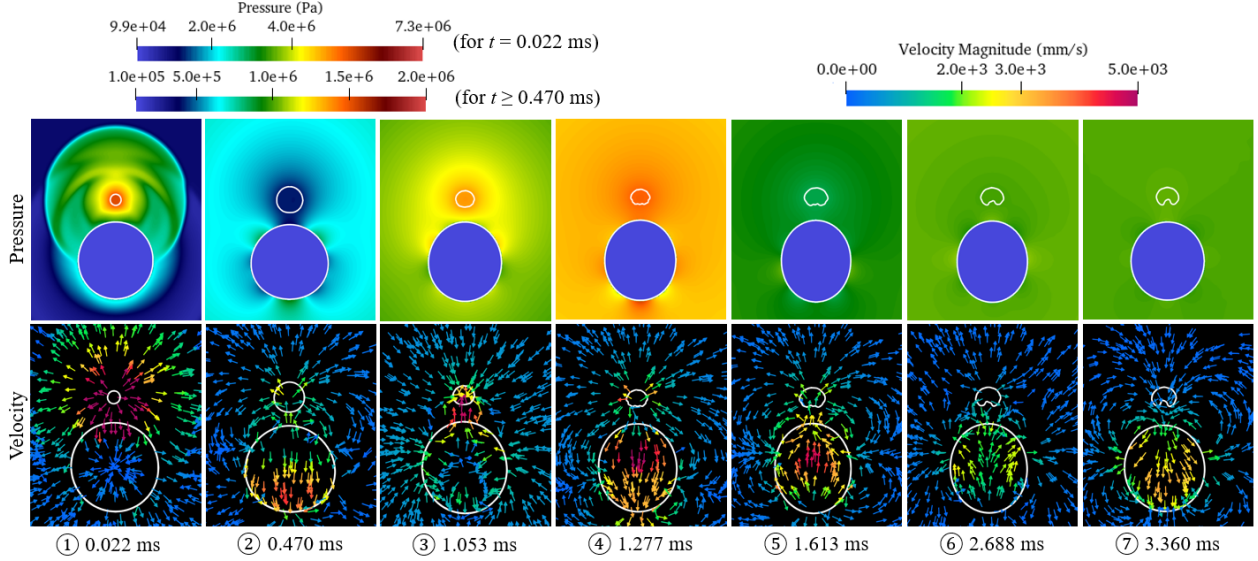
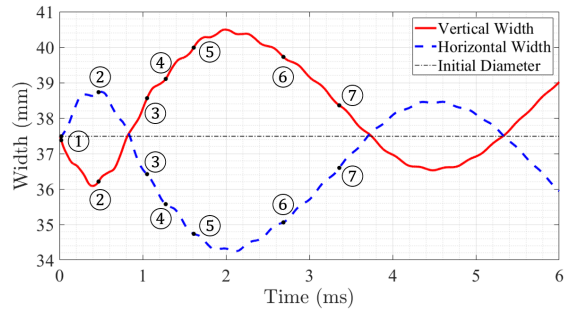
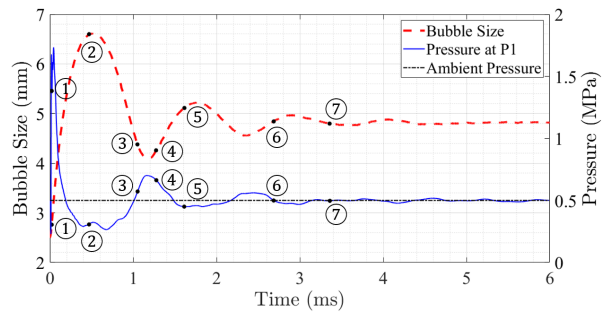


Figure 9: Snapshots of the fluid and structural results in the case of  $p_0 = 8.0$  MPa.

345 decreases. At this time, the cylinder starts to bounce back from the vertical  
 compression, which drives the volume of water above it to move towards the  
 bubble. This again indicates that the bubble dynamics is affected by the tran-  
 sient structural deformation. After  $t = 0.528$  ms, the bubble starts to contract.  
 In accordance with the vertical stretch of the cylinder, a high pressure region  
 350 occurs between the bubble and the structure at around 0.65 ms, which causes  
 an increased vertical pressure gradient that accelerates the upward water flow at  
 the bubble's bottom surface. Although this vertical pressure gradient gradually  
 decreases and reverses direction at around 1 ms, the accelerated contraction of  
 the bubble's bottom surface continues due to the inertia of water. Sub-figure ③  
 355 is taken at  $t = 1.053$  ms, when the bubble is about to reach its minimum size.  
 From the velocity field, the faster contraction of the bubble's bottom surface  
 can still be observed. Sub-figure ③ also shows that as the bubble's contraction  
 slows down, the local pressure increases. This increase is captured by sensor P1  
 as a pressure pulse around 1.2 ms (Figure 10(b)). At  $t = 1.193$  ms, the bubble  
 360 contracts to its first minimum size and begins to expand again. Sub-figure ④



(a)



(b)

Figure 10: Time history of selected quantities of interest in the case of  $p_0 = 8.0$  MPa. (a) The distances between the top and bottom points (i.e. vertical width) and the left and right points (i.e. horizontal width) of the cylinder. (b) The bubble size (radius equivalent) and the fluid pressure at a sensor location. The time instants shown in Figure 9 are marked on these curves.

is taken at  $t = 1.277$  ms. From this time onward, the bubble's shape becomes clearly non-spherical. The last three sub-figures are taken during the second and third cycles of bubble oscillation (i.e. expansion and contraction). The pressure variation becomes smaller both in time and in space. A dent gradually develops  
365 at the bottom of the bubble, which can be attributed to both the reflection of the incident shock wave against the structural surface and the accelerated upward water flow generated by the high vertical pressure gradient between the bubble and the cylinder.

In this test case, the structural deformation is relatively small. Yielding  
370 only occurs on the outer and inner surfaces of the top, bottom, left, and right points of the cylinder, with the maximum value of effective plastic strain less than  $2.0 \times 10^{-3}$ . Figure 10(a) shows that although some higher frequency vibration modes are activated by the non-uniform hydrodynamic loads, the structural deformation is dominated by the first asymmetric breathing mode, which  
375 features alternative compression and expansion in vertical and horizontal directions [46, 47]. This figure also indicates that both the mean configuration of the cylinder and the configuration with the largest deformation (at around 2.0 ms) have an ellipsoidal shape, with the primary (longer) axis in the vertical direction. In other words, the result indicates a tendency of collapsing into a  
380 horizontally compressed configuration.

#### 4.2. $p_0 = 12.5$ MPa (enthalpy 0.8590 J/mm)

When the initial pressure inside the bubble is increased to 12.5 MPa, the cylinder collapses in an orientation that features vertical extension and horizontal compression. This case has been briefly discussed in Section 3 to demonstrate  
385 mesh convergence. Figure 11 shows six (6) solution snapshots, which illustrates the evolution of the bubble, the cylinder, and the fluid pressure and velocity fields. The cylinder's effective plastic strain is also visualized in the upper-row images. Again, the cylinder's horizontal and vertical widths are calculated to characterize its deformation (Figure 12(a)). The time histories of bubble size  
390 and fluid pressure at a sensor location (P1 in Figure 4) are shown in Figure 12(b).

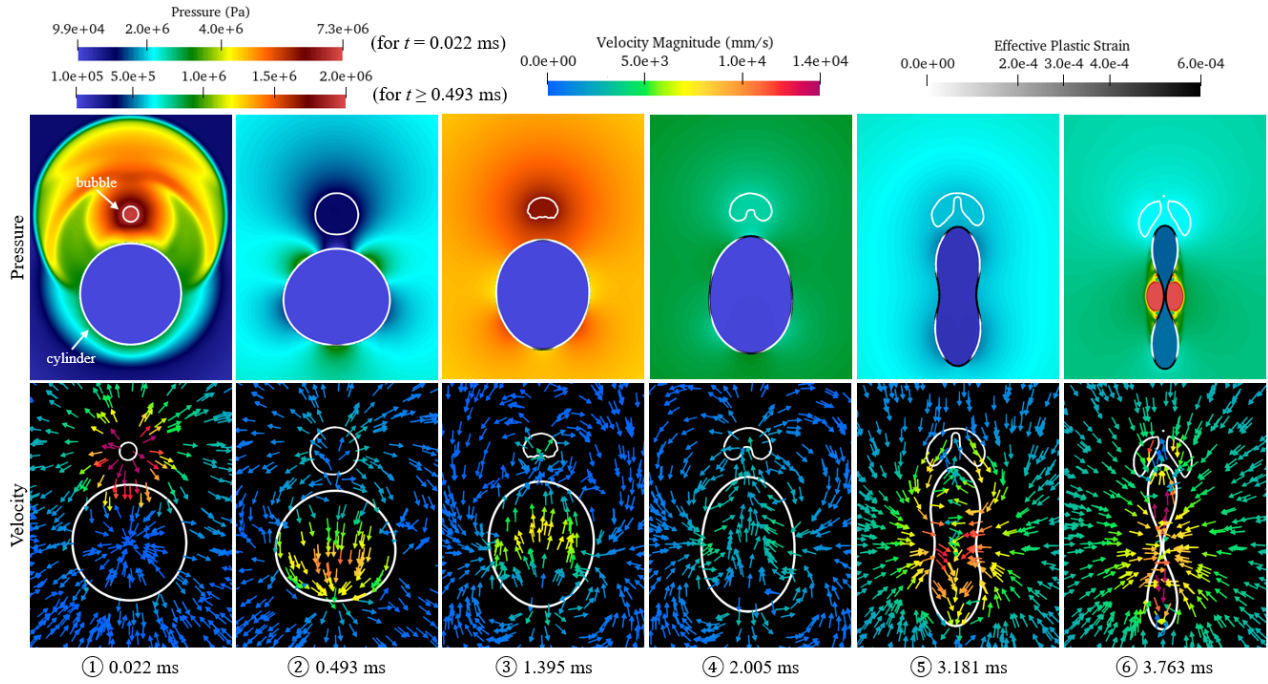
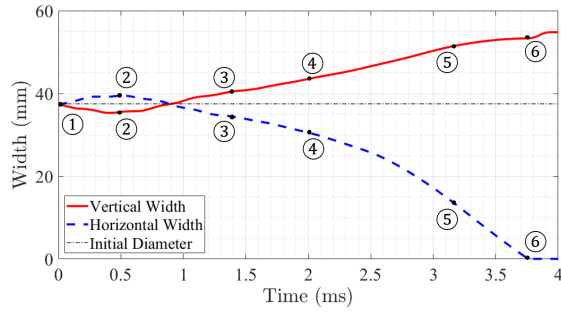


Figure 11: Snapshots of the fluid and structural results in the case of  $p_0 = 12.5$  MPa.

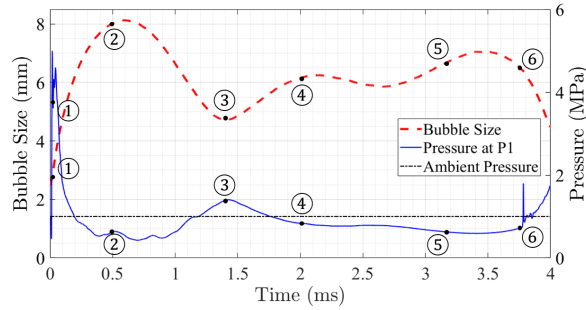
In Figure 11, the first snapshot is taken at  $t = 0.022$  ms, the same time as Figure 9①. From the pressure field, it can be observed that the incident shock wave and its reflection both have a higher magnitude compared to the previous case ( $p_0 = 8.0$  MPa). Again, the cylinder is compressed in the vertical direction due to both the shock load and the water flow generated by the expanding bubble. The compression stops at around 0.4 ms, before the bubble reaches its maximum size (Figure 12). Sub-figure ② is taken at  $t = 0.493$  ms, when the structure is bouncing back in the vertical direction, while the bubble is still expanding. As a result, the downward expansion of the bubble is hindered by the structure. Unlike the previous case, a small amount of plastic deformation (effective plastic strain:  $1.34 \times 10^{-3}$ ) has already developed at this time at the bottom of the cylinder.

The bubble reaches its maximum size at  $t = 0.569$  ms. Then, it starts to contract. Figure 11③ is taken at  $t = 1.395$  ms, when the bubble reaches





(a)



(b)

Figure 12: Time history of selected quantities of interest in the case of  $p_0 = 12.5$  MPa. (a) The distances between the top and bottom points and the left and right points of the cylinder. (b) The bubble size (radius equivalent) and the fluid pressure at a sensor location. The time instants shown in Figure 11 are marked on these curves.

405 its minimum size. Again, a pressure pulse is generated by the bubble, which elevates the pressure around the cylinder (also see Figure 12(b)). At this time, the cylinder is still stretched in the vertical direction and compressed in the horizontal direction (Figure 12(a)). The elevated pressure field enhances its horizontal compression. Afterwards, the cylinder continues to deform in the  
 410 same mode, instead of bouncing back as in the previous case. Sub-figures ③④⑤ illustrate this process. Therefore, the result suggests that the second pressure pulse generated by the contraction of the bubble have a significant impact on the cylinder's mode of collapse.

Besides changing the collapse behavior of the cylinder, the increased initial

415 pressure also influences the bubble dynamics through a complex dynamic inter-  
 action between the bubble and the cylinder. Like in the previous case, a dent  
 forms at the bubble’s bottom surface. In the present case, this dent gradually  
 evolves into a liquid “jet” during the process of the cylinder’s collapse. The  
 jet penetrates the upper surface of the bubble at 3.46 ms (see Figure 11, Sub-  
 420 figures ⑤ and ⑥). In the literature of cavitation, it is well-known that a bubble  
 collapsing near a *rigid* surface often generates a liquid jet towards the surface,  
 which can be an important mechanism of material damage [48, 42, 49, 50, 16].  
 It should be noted that the jet observed in the current simulation is in the  
 opposite direction, and its formation is closely related to the deformation of  
 425 the cylinder. This type of “counter jet” has also been observed previously in  
 experiments that involve underwater explosion near an elastic solid body [21].

Figure 12(a) shows that starting at around 1.2 ms, the speed of the cylinder’s  
 horizontal compression keeps increasing. The collapse of the cylinder pulls the  
 surrounding water towards it, which can be observed in the fluid velocity field  
 430 in Figure 11, Sub-figures ⑤ and ⑥. At  $t = 3.763$  ms, the cylinder reaches self-  
 contact. An implosion shock wave is emitted at the point of contact because  
 the inward motion of the surrounding water is suddenly stopped. This shock  
 wave is also captured at sensor P1 (Figure 12(b)).

A comparison between Figures 12(b) and 10(b) reveals that as  $p_0$  increases,  
 435 the bubble’s period of oscillation also increases. For example, the time when the  
 bubble reaches the second maximum size is approximately 2.15 ms in the current  
 case, compared to 1.76 ms in the previous case. This trend is consistent with  
 simplified bubble dynamics models that assume spherical symmetry (e.g. [1, 51]).

#### 4.3. $p_0 = 25.0$ MPa (enthalpy 1.7181 J/mm)

440 The initial pressure inside the bubble is increased further to 25.0 MPa in this  
 case. Figure 13 presents six (6) solution snapshots. Figure 14 shows the time  
 histories of the cylinder’s deformation, the bubble size, and the fluid pressure at  
 the same sensor location. It is found that the cylinder collapses in an orientation  
 that is perpendicular to the one observed previously in the case of 12.5 MPa.

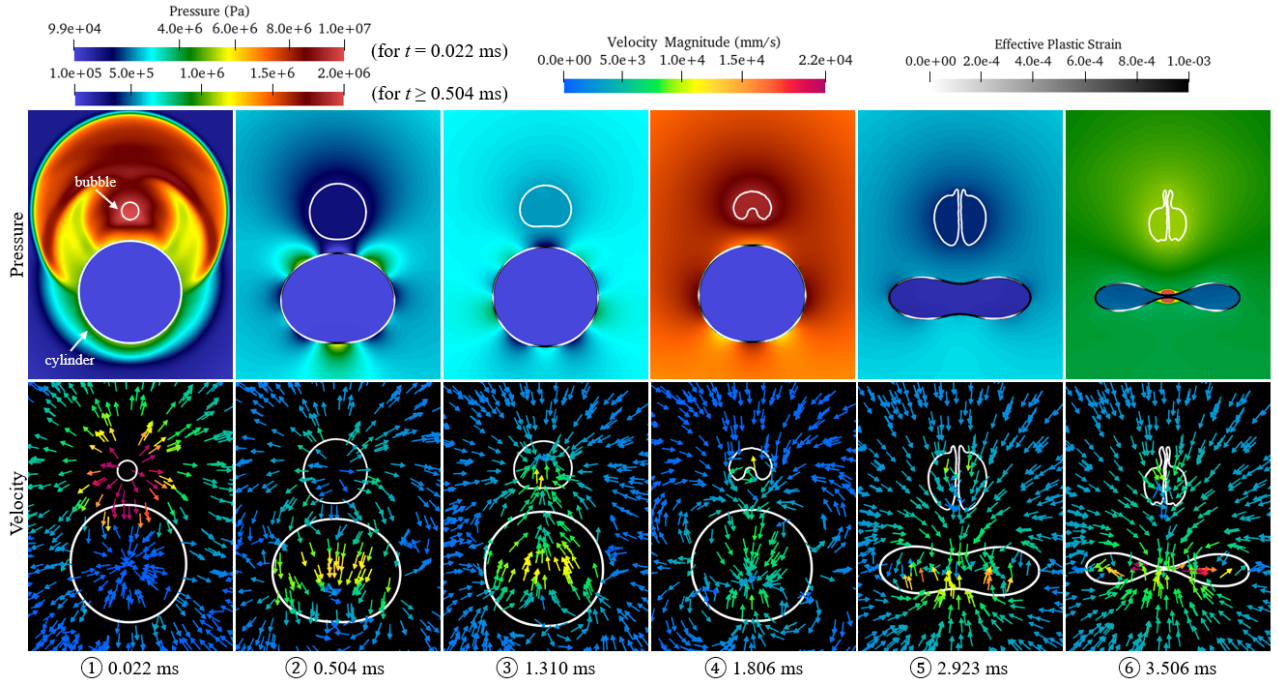
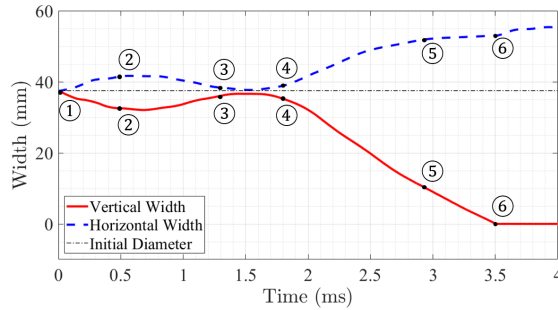


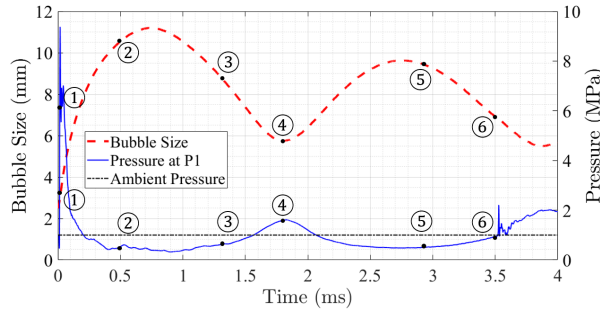
Figure 13: Snapshots of the fluid and structural results in the case of  $p_0 = 25.0$  MPa.

445 Due to the higher initial pressure inside the bubble, both the incident and  
the reflected shock waves have a higher magnitude (Figure 13①). Sub-figure ②  
is taken at  $t = 0.504$  ms, when the bubble is expanding and the cylinder being  
compressed in the vertical direction. At this time, plastic deformation has  
already developed at the top, bottom, left, and right points of the cylinder,  
450 which can be observed from the visualization of effective plastic strain. The  
cylinder's vertical compression stops at  $t = 0.68$  ms, before the bubble reaches its  
maximum size. Then, the cylinder starts to bounce back. Unlike all the previous  
cases, in this case the cylinder cannot recover its original circular configuration,  
because of the developed plastic deformation. This is evident in Figure 14(a), as  
455 the two curves never cross after  $t = 0$  ms. Figure 13③ is taken at  $t = 1.310$  ms,  
when the cylinder is expanding vertically while the bubble is contracting. It can  
be seen that the bottom of the bubble is flattened by the flow induced by the  
cylinder's vertical expansion. The vertical expansion and horizontal contraction

of the cylinder stop at 1.445 ms. Then, the cylinder starts to deform in the  
 460 opposite way.



(a)



(b)

Figure 14: Time history of selected quantities of interest in the case of  $p_0 = 25.0$  MPa. (a) The distances between the top and bottom points and the left and right points of the cylinder. (b) The bubble size (radius equivalent) and the fluid pressure at a sensor location. The time instants shown in Figure 13 are marked on these curves.

Because of the increased initial pressure ( $p_0$ ), the bubble's period of oscillation increases. It is at  $t = 1.806$  ms that the bubble contracts to its minimum size, compared to  $t = 1.395$  ms in the previous case. Sub-figure ④ in Figure 13 is taken at this time. Same as the previous cases, the contraction of the bubble  
 465 generates a pressure pulse that elevates the pressure field around the cylinder. Nonetheless, in this case the delayed pressure pulse meets a cylinder that has a different configuration, that is, vertically compressed and horizontally stretched. As a result, the pressure pulse promotes the vertical compression of the cylinder.

After this time, the cylinder loses stability and starts to collapse. Sub-figures ⑤  
470 and ⑥ are taken during this process.

In this case, the bubble also produces a counter jet pointing away from the  
cylinder. This liquid jet keeps growing as the cylinder collapses, and it pene-  
trates the upper surface of the bubble at  $t = 2.509$  ms. Compared to the previous  
case, the jet is narrower and longer. When the cylinder is compressed vertically  
475 during the bubble's expansion phase after 1.806 ms, the bubble's lower sur-  
face expands faster than other regions, which elongates the bubble downwards.  
Sub-figure ⑥ in Figure 13 is taken at the instant that the cylinder reaches  
self-contact. Again, the emission of an implosion shock wave can be clearly  
observed from the pressure field. It is notable that the collapsed configuration  
480 of the cylinder is symmetric with respect to its horizontal mid-plane (i.e. the  
middle  $x$ - $z$  plane), despite that the external load is highly asymmetric.

In addition, the cylinder collapses into a configuration that features verti-  
cal compression and horizontal expansion. Although this is a different mode  
compared to the previous case of  $p_0 = 12.5$  MPa, the result shows that in both  
485 cases, the mode of collapse is determined at the time the bubble reaches its min-  
imum size. The difference in collapse mode can be explained by the different  
configurations of the cylinder at this time. Specifically, in this case, the cylinder  
is vertically compressed and horizontally stretched, whereas in the case with  
 $p_0 = 12.5$  MPa, it is vertically stretched and horizontally compressed. Further-  
490 more, the result suggests that the difference in the cylinder's configuration at  
the arrival of the pressure pulse is related to both the increase of the bubble's  
period of oscillation and the cylinder's plastic deformation.

#### 4.4. $p_0 = 50.0$ MPa (enthalpy 3.4361 J/mm)

In this case, the cylinder collapses into another shape that is noticeably  
495 different from those observed in the cases of  $p_0 = 12.5$  MPa and  $p_0 = 25$  MPa.  
The same set of results are extracted and presented in Figures 15 and 16.

In Figure 15, sub-figure ① is taken at the same time as in the previous  
cases, which highlights the initial loads from the bubble including a shock wave

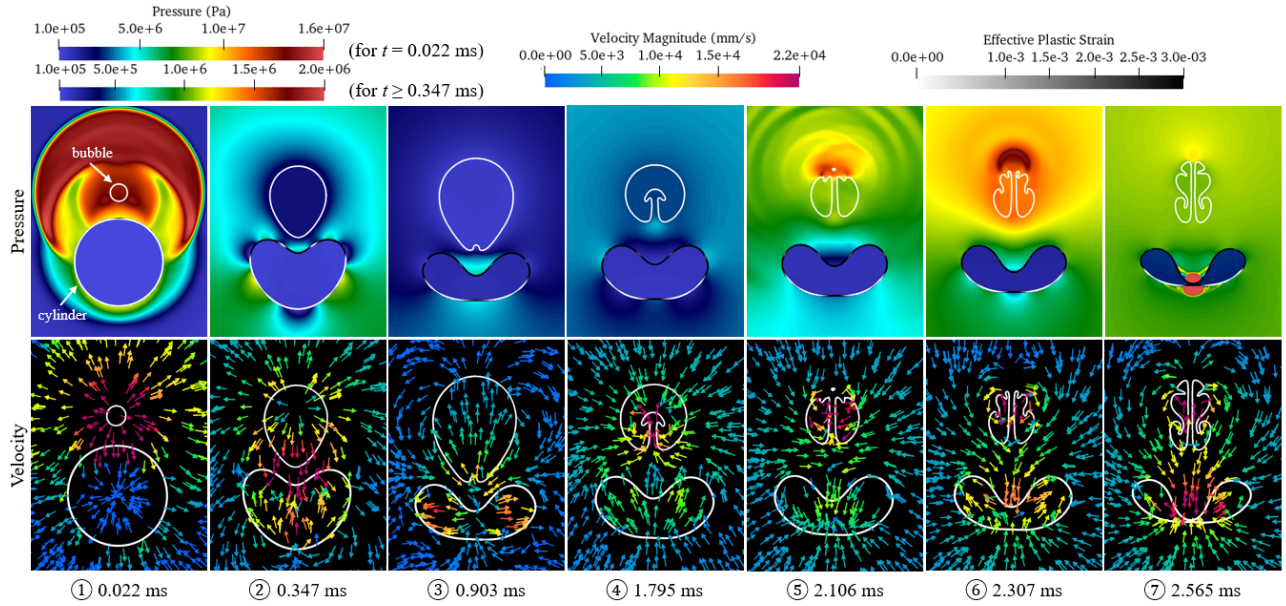


Figure 15: Snapshots of the fluid and structural results in the case of  $p_0 = 50.0$  MPa.

with pressure of the order of 20 MPa and a water flow with velocity of the  
 500 order of  $4 \times 10^4$  mm/s. At  $t = 0.347$  ms (Sub-figure ②), the result is already  
 very different from the previous cases. Both the bubble and the cylinder are  
 no longer symmetric with respect to their horizontal mid-planes (i.e. the middle  
 $x$ - $z$  plane). The top region of the cylinder is collapsing, while the bottom region  
 has much smaller, elastic deformation. Despite a higher initial pressure ( $p_0$ )  
 505 compared to the previous case, yielding in the bottom region of the cylinder is  
 delayed. Sub-figure ② also shows that the bubble deforms into an oval shape,  
 as its bottom region is pulled by a downward velocity field that is in accordance  
 with the collapse of the cylinder.

Sub-figure ③ is taken at  $t = 0.903$  ms. Around this time, the collapse of the  
 510 cylinder stops, despite that its vertical width has dropped by over 70% compared  
 to the original configuration (Figure 16(a)). Figure 16(b) shows that this is the  
 time when the bubble has reached its maximum size and starts to contract. The  
 contraction of the bubble is an inertial effect, caused by the continuous decrease

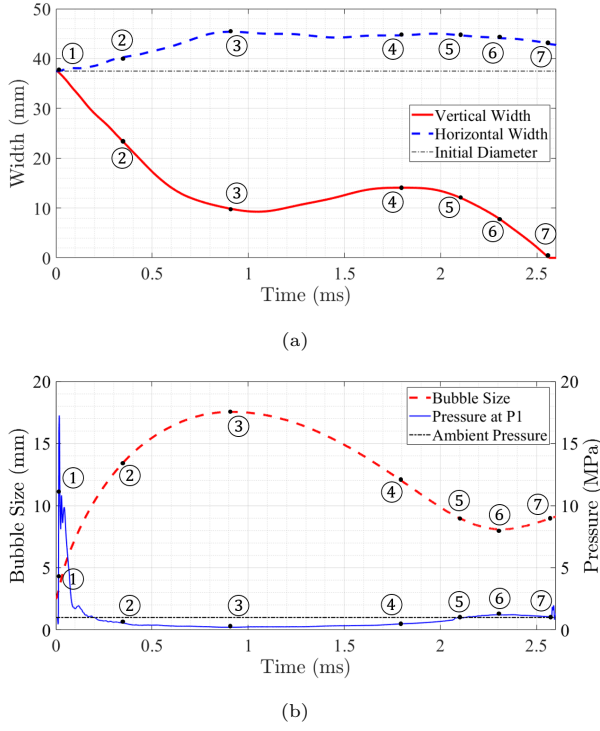


Figure 16: Time history of selected quantities of interest in the case of  $p_0 = 50.0$  MPa. (a) The distances between the top and bottom points and the left and right points of the cylinder. (b) The bubble size (radius equivalent) and the fluid pressure at a sensor location. The time instants shown in Figure 15 are marked on these curves.

of the internal pressure during the bubble's expansion. It pulls the surrounding  
 515 water towards it, thereby facilitating the formation of the velocity field that  
 stops the downward collapse of the cylinder. Similar to the previous cases, a  
 dent can be observed at the bottom of the bubble, which gradually evolves into  
 an upward liquid jet. Sub-figure ④ is taken at  $t = 1.795$  ms, when the collapse  
 of the cylinder resumes. As the cylinder collapses, the liquid jet continues  
 520 penetrating the bubble. Sub-figure ⑤ is taken at  $t = 2.106$  ms, shortly after  
 the jet penetrates the top surface of the bubble. At  $t = 2.307$  ms, the bubble  
 contracts to its minimum size (Sub-figure ⑥). Finally, at  $t = 2.565$  ms, the  
 cylinder reaches self-contact (Sub-figure ⑦). Again, an implosion shock wave is

generated at the point of contact.

525 In summary, because of the higher initial pressure ( $p_0$ ), the collapse of the cylinder starts at an earlier time compared to the previous two cases (12.5 MPa and 25 MPa), and it starts only in the top region, which is close to the bubble. In addition, the collapse of the cylinder does not progress in a monotonic fashion. Instead, it is temporarily pulled back as the bubble contracts, which again  
530 indicates a strong coupling between the bubble dynamics and the cylinder's transient deformation. At the end, when the cylinder reaches self-contact, its configuration is clearly different from the shape observed in the case of  $p_0 = 25$  MPa in that it is no longer symmetric with respect to the horizontal mid-plane (i.e. the middle  $x$ - $z$  plane).

#### 535 4.5. $p_0 = 100.0$ MPa (enthalpy 6.8722 J/mm)

In this case, the cylinder collapses into a configuration similar to the one observed in the previous case. The main difference is that the collapse progresses monotonically, and is not interrupted by the bubble. The results are presented in Figures 17 and 18.

540 In Figure 17, Sub-figure ① is taken at 0.022 ms, the same time instant as in the previous cases. At this time, yielding has started not only in the top region of the cylinder, but also in its bottom region. The pressure field shows that the incident shock wave (i.e. the region that has red color and a crescent shape) has not reached the bottom of cylinder through water. Therefore, the yielding of  
545 the bottom region should be attributed to the convergence of the stress waves propagating downward along the two sides of the cylinder. Sub-figure ② is taken at  $t = 0.034$  ms, when the reflected shock wave has just passed the sensor location P1. This reflection is captured by the sensor as the second, smaller pressure spike (Figure 18(b)). At this time, plastic deformation has already developed around the entire circumference of the cylinder. Sub-figure ③ is  
550 taken at 0.202 ms. At this time, the top region of the cylinder is highly concave. Again, the bottom region of the bubble is pulled by the downward velocity field created by the collapsing cylinder. As a result, it deforms into an oval shape.



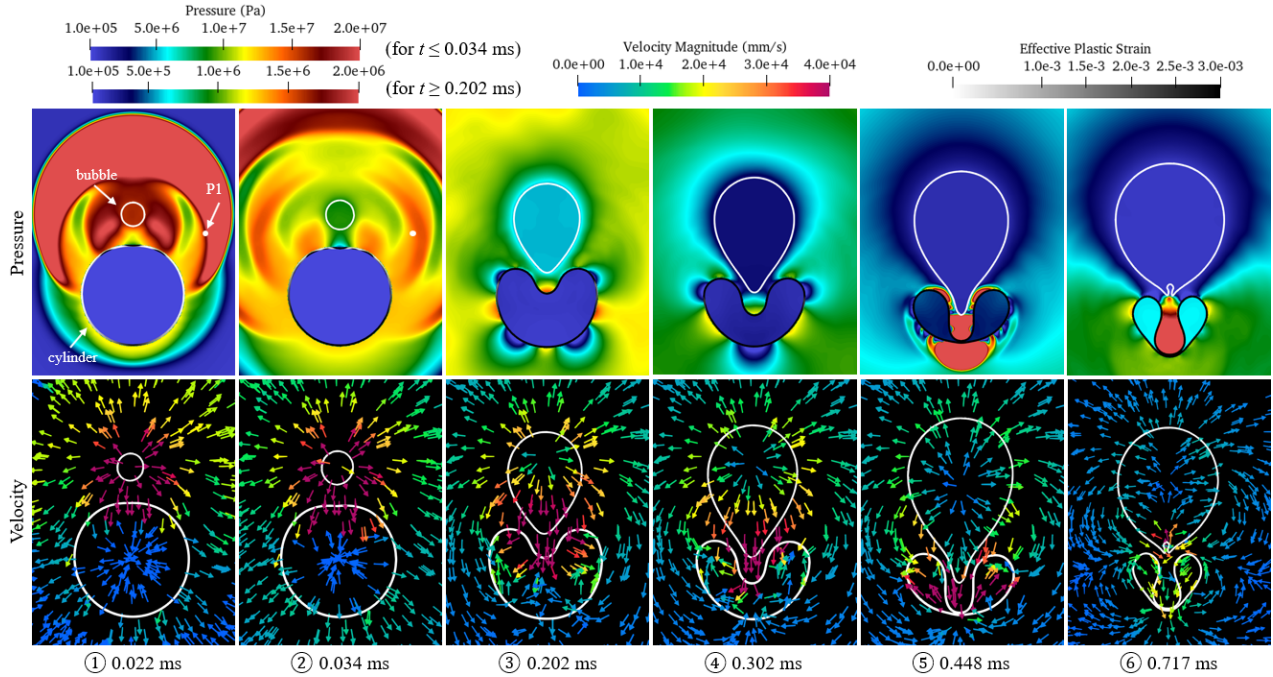


Figure 17: Snapshots of the fluid and structural results in the case of  $p_0 = 100.0$  MPa. The sensor location P1 is marked in the first two sub-figures.

Sub-figure ④ is taken at 0.302 ms. From Figure 18(a) it can be observed  
555 that until this time, the horizontal width of the cylinder has largely remained  
constant. Afterwards, it starts to decrease, as the two lobes of the cylinder fold  
towards each other. This is different from the last two cases ( $p_0 = 25$  MPa  
and 50 MPa) as in those cases, the horizontal width increases as the cylinder  
collapses. At  $t = 0.448$  ms (sub-figure ⑤), the cylinder reaches self-contact  
560 and emits an implosion shock wave. The bubble is still expanding at this time  
instant. Lastly, Sub-figure ⑥ is taken at  $t = 0.717$  ms. Again, a liquid jet forms  
at the bottom of the bubble, and it will gradually penetrate the bubble.

In this case, the cylinder collapses within 0.5 ms, a time interval that is  
much shorter than the previous cases. On the other hand, the bubble's period  
565 of oscillation is longer because of the higher initial pressure ( $p_0$ ). As a result of  
these changes, the bubble keeps expanding during the entire collapsing process

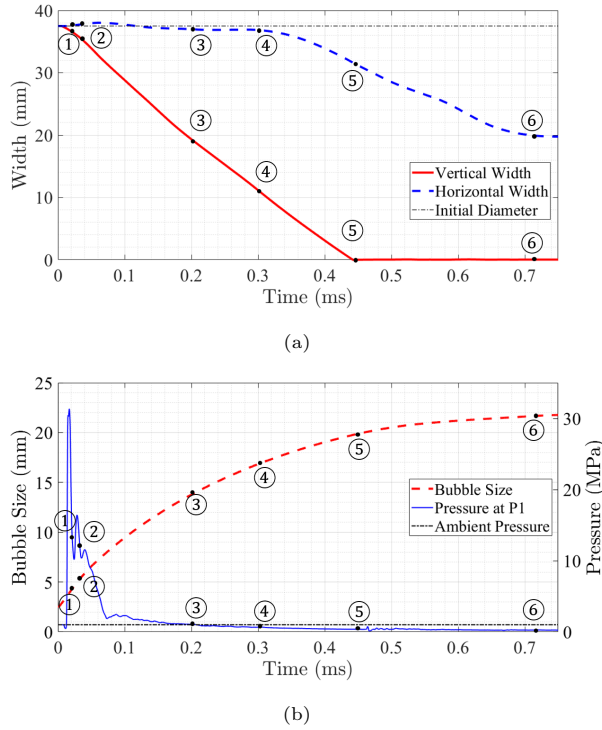


Figure 18: Time history of selected quantities of interest in the case of  $p_0 = 100.0$  MPa. (a) The distances between the top and bottom points and the left and right points of the cylinder. (b) The bubble size (radius equivalent) and the fluid pressure at a sensor location. The time instants shown in Figure 17 are marked on these curves.

of the cylinder (Figure 18(b)). Since bubble contraction does not happen during the collapse of the cylinder, the cylinder does not rebound like in the previous case ( $p_0 = 50$  MPa).

570 *4.6. Summary*

We have discussed five (5) representative cases with different initial pressure inside the bubble ( $p_0$ ). The results show that the collapse behavior of the cylinder can be drastically different as  $p_0$  varies, while all the other parameters remain fixed. Figure 19 presents a comparison of all the five cases in terms  
 575 of structural deformation and bubble dynamics. In this figure, the time axis is synchronized among all the cases. For each case, the ticks on the time axis

mark the start and end times of the bubble's half cycles, i.e. the expansion and contraction phases. One image is presented within each time interval, in which the bubble and the cylinder's configuration at different time instants are  
580 superimposed. The time evolution is shown using opacity. Specifically, a darker line corresponds to a result at a later time. The time interval between adjacent time instants is fixed within each image. The dashed curly brackets along the time axis represent the time span of each image.

In the first case ( $p_0 = 8.0$  MPa), due to the low pressure inside the bubble,  
585 the cylinder vibrates without collapsing. As  $p_0$  increases, in the second case ( $p_0 = 12.5$  MPa) the cylinder collapses into a configuration that features horizontal compression and vertical extension. The top of the cylinder, which is closest to the bubble, is found to move towards the bubble. In the third case ( $p_0 = 25.0$  MPa), the cylinder collapses into a configuration that features verti-  
590 cal compression and horizontal extension, that is, a configuration perpendicular to that observed in the second case. Notably, in both cases, the collapsed configuration is symmetric with respect to the cylinder's horizontal mid-plane (i.e. the middle  $x$ - $z$  plane), despite the fact that the loading is clearly asymmetric. In the fourth case ( $p_0 = 50.0$  MPa), the cylinder is still vertically compressed after  
595 collapsing but the aforementioned symmetry is lost. The deformation mostly occurs at the top region of the cylinder. Moreover, the cylinder does not collapse monotonically. It is pulled back by the bubble during a short period of time when bubble is contracting. In the last case ( $p_0 = 100.0$  MPa), the cylinder collapses monotonically within a very short period of time. It reaches self-contact  
600 before the bubble completes the first expansion phase.

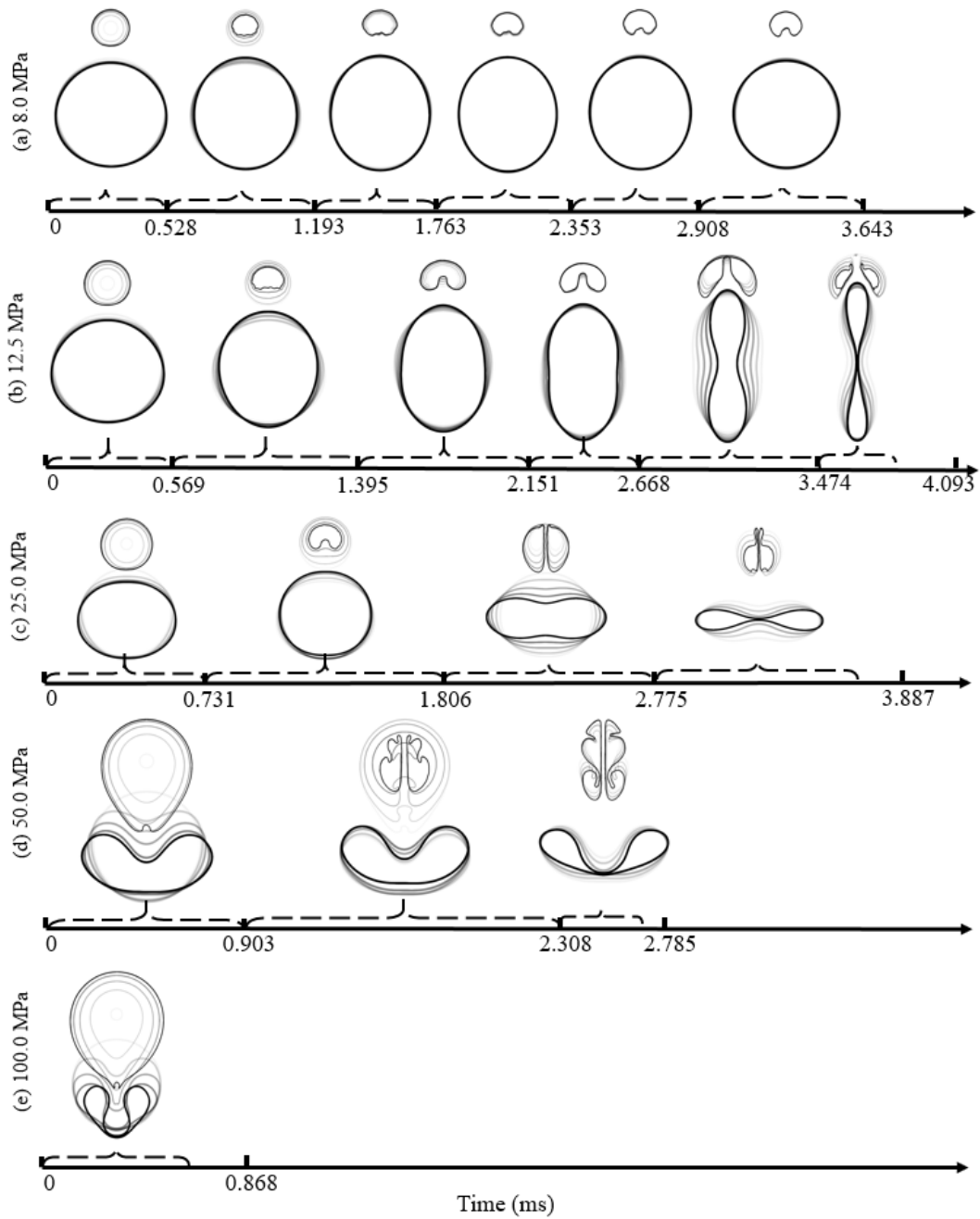


Figure 19: Comparison of the evolution of the bubble and the cylinder in the five (5) representative cases. One image is generated for each half cycle (expansion or contraction) of the bubble. Within each image, results at different time instants are superimposed, and the increase of opacity indicates the time evolution.

## 5. Transition of collapse modes

In this section, we discuss the different types of collapse behaviors using a bigger data set that consists of 15 simulations in which  $p_0$  is varied from 1.0 MPa to 100.0 MPa. The transition among different modes of collapse are investigated.

### 5.1. Different collapse behaviors

Figure 20 summarizes the different collapse behaviors observed in this parametric study. In the remainder of this paper, the mode of collapse that features symmetric horizontal compression is referred to as Mode 2A. The mode of collapse that features symmetric vertical compression is referred to as Mode 2B. The asymmetric collapse with vertical compression is referred to as Mode 2C. Here, the number 2 refers to the fact that the collapsed configuration contains two lobes. In addition, Figure 21 presents the mode of collapse observed in each test case, as well as the time it takes for the cylinder to reach self-contact, denoted by  $t_{co}$ .

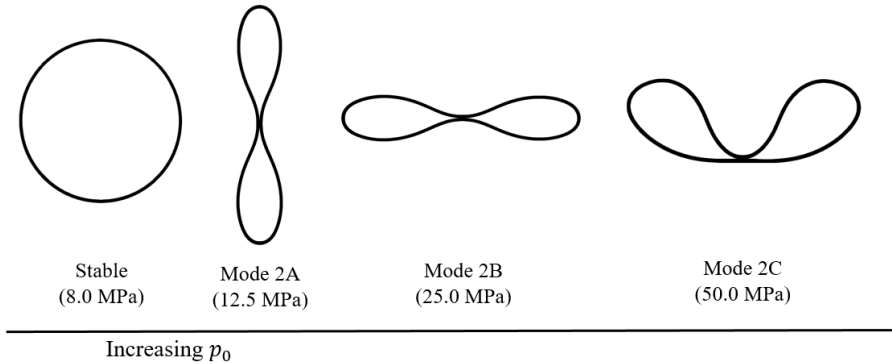


Figure 20: The transition of collapse modes as  $p_0$  increases from 1 MPa to 100 MPa.

A few findings from this parametric study are noteworthy.

- (1) As pressure  $p_0$  increases, the first collapse mode (Mode 2A) features horizontal compression and vertical extension.

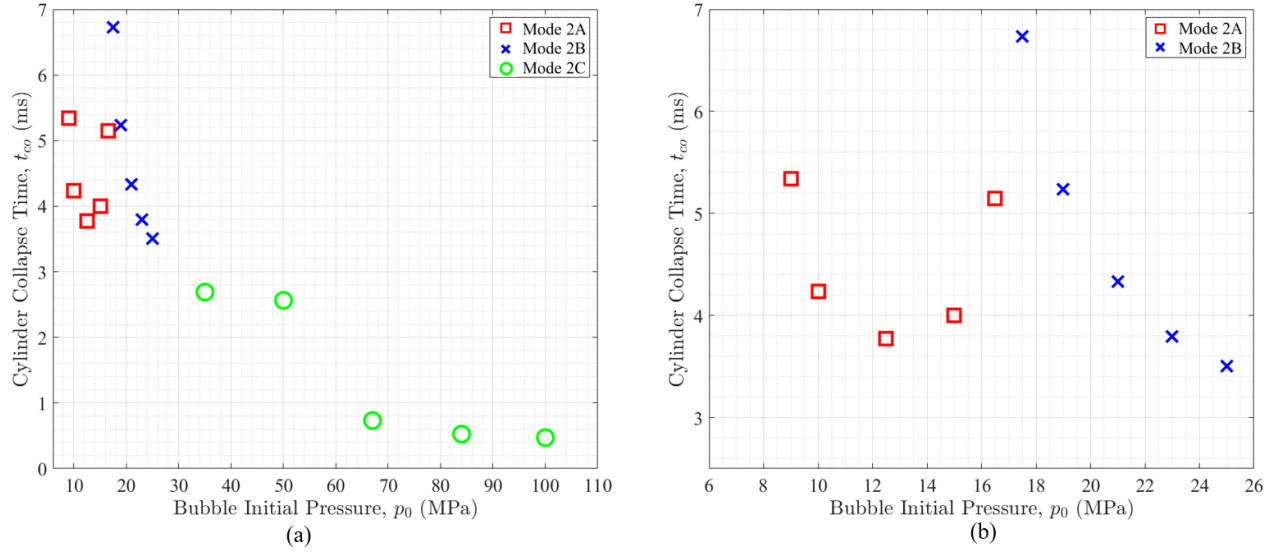


Figure 21: The time to collapse ( $t_{co}$ ) for (a)  $8 \text{ MPa} < p_0 \leq 100.0 \text{ MPa}$  and (b)  $8 \text{ MPa} < p_0 \leq 25 \text{ MPa}$ .

- (2) The time to collapse,  $t_{co}$ , is not a monotonically decreasing function of  $p_0$ ,  
 620 despite that a larger  $p_0$  generally means a stronger load.
- (3) As  $p_0$  increases beyond 16.5 MPa, a change of collapse mode (from Mode  
 2A to Mode 2B) is observed.

## 5.2. Discussion

To explain the findings mentioned above, it is helpful to examine the time  
 625 history of plastic strain in the cylinder. Figure 22 presents the effective plastic  
 strain measured at the top and bottom points of the cylinder's inside wall.  
 From Figure 22(a), it is clear that Mode 2A collapse is not induced directly by  
 the initial loads, i.e. the incident shock wave and the water flow caused by the  
 bubble's initial expansion. For example, in the cases of  $p_0 = 12.5 \text{ MPa}$  and  
 630  $15.0 \text{ MPa}$ , the effective plastic strain remains zero (or nearly zero) until 1 ms,  
 when the initial loads have long passed. In both cases, plastic strain starts to  
 develop after 1.5 ms, when the surrounding water pressure is elevated due to the  
 bubble's contraction (cf. Figures 11 and 12). Therefore, the first collapse mode

is induced mainly by the first contraction phase of the bubble and the resulting  
 635 pressure pulse. Around this time, the cylinder happens to be in a configuration  
 of vertical extension and horizontal compression, which determines the shape of  
 Mode 2A collapse.

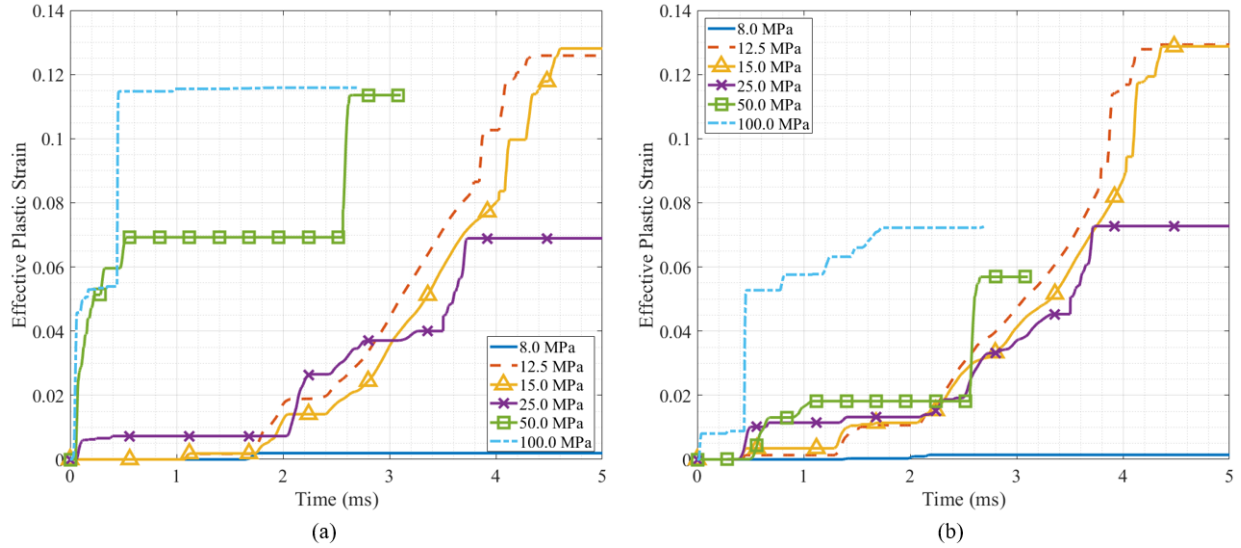


Figure 22: Effective plastic strain at the (a) top point and (b) bottom point of the cylinder's inside wall.

Figure 21(b) shows that for the cases that result in Mode 2A collapse, the  
 time to collapse ( $t_{co}$ ) does not decrease monotonically as  $p_0$  increases. Specifi-  
 640 cally, when  $p_0$  is increased from 12.5 MPa to 15.0 MPa, the cylinder collapses  
 slower. This phenomenon is related to the plastic deformation caused by the  
 initial loads. Figure 22(b) shows that, in the cases of  $p_0 = 12.5$  MPa and  
 $p_0 = 15.0$  MPa, there is a small amount of plastic deformation at the bottom  
 of the cylinder around 0.5 ms. Around this time, the cylinder's vertical width  
 645 reaches a minimum value. In other words, the cylinder has just completed the  
 first half-cycle of vibration, which results directly from the initial loads (cf. Fig-  
 ure 12(a)). Figure 23 provides a cross comparison of the plastic deformation  
 induced by the initial loads among all the test cases. It is clear that as  $p_0$  in-  
 creases, the effective plastic strain also increases. As discussed in Section 4.3,

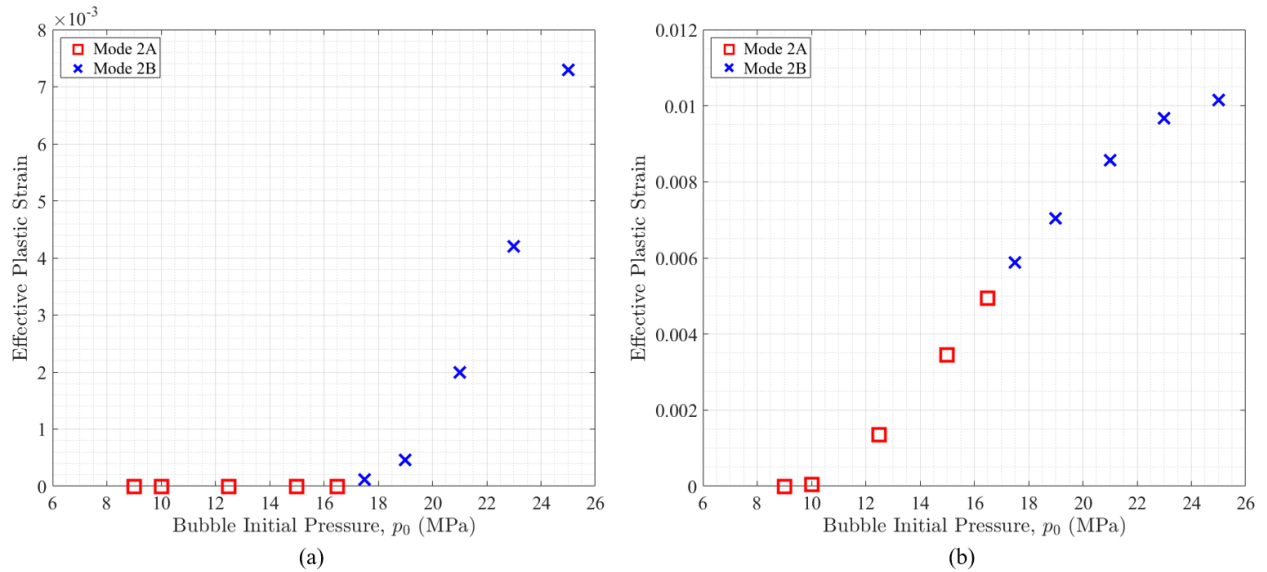


Figure 23: Effective plastic strain at the cylinder inside wall's (a) top and (b) bottom points when the cylinder's vertical width reaches minimum for the first time (i.e. when the cylinder completes the first half-cycle of vibration).

650 such plastic deformation tends to hinder Mode 2A collapse. Therefore, the result shows that the increased plastic deformation due to stronger initial loads is a factor that increases the cylinder's time to collapse ( $t_{co}$ ) in Mode 2A.

The increase of plastic deformation caused by the initial loads also leads to the fact that when the cylinder completes its first cycle of vibration, it can  
 655 no longer recover the initial configuration. Instead, it is vertically compressed and horizontally stretched. Figure 24 shows that as  $p_0$  further increases beyond 12.5 MPa, the vertical width of the cylinder decreases monotonically. As described in Section 4, when the cylinder completes its first cycle of vibration, it is subjected to a pressure pulse that results from the contraction of the bubble.  
 660 This pressure pulse drives the cylinder to collapse in the vertical direction. In summary, the results suggest that Mode 2B collapse is triggered by the initial loads and facilitated by the bubble's dynamics, particularly its first contraction phase that generates the second pressure pulse.



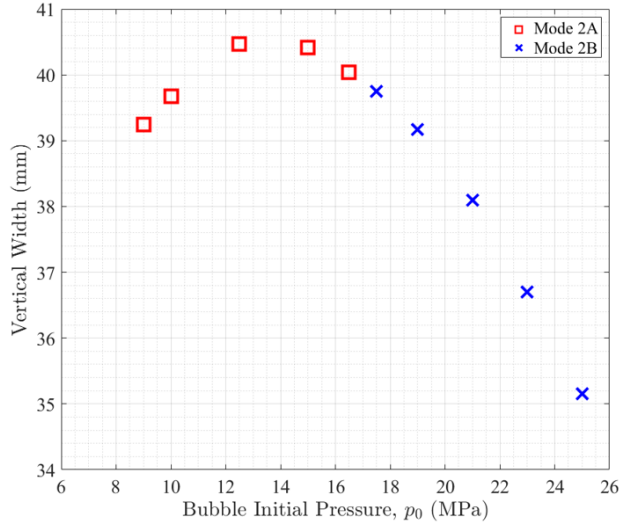


Figure 24: Vertical width of the cylinder when the bubble contracts to its minimum size.

In addition of the findings listed in Section 5.1, in Figure 21, it can be seen  
 665 that when the cylinder collapses in Mode 2C, there is a sudden decrease of  $t_{co}$   
 between  $p_0 = 50.0$  MPa and  $67.0$  MPa. This behavior is related to the time  
 sequence of cylinder collapse and bubble contraction, as discussed in Section 4.4  
 and Section 4.5.

## 6. Conclusion

670 The collapse of an underwater aluminum cylinder due to a near-field explo-  
 sion is investigated using fluid-structure coupled simulations. Previous studies  
 in this area suggest that the dynamics of the explosion bubble may have a sub-  
 stantial effect in this type of events. Nonetheless, knowledge about this effect  
 is very limited. Therefore, a specific objective of this study is to capture and  
 675 explain the two-way interaction between the explosion bubble and the structure,  
 using a two-dimensional model problem.

The computational model employed in this study combines a multiphase  
 compressible fluid dynamics solver with a nonlinear structural dynamics solver.  
 It has been verified and validated for several problems that are closely related

680 to the current work, including the collapse of aluminum cylinders due to hydro-  
static pressure, and the pulsation of bubbles in free field and near solid materials.  
In this work, we start with a mesh convergence analysis in which the fluid and  
structural meshes are progressively refined until convergence is achieved. After-  
wards, a parametric study is conducted, in which the initial pressure inside the  
685 explosion bubble ( $p_0$ ) is varied by two orders of magnitude. The interaction of  
the bubble, the surrounding liquid water, and the aluminum cylinder is investi-  
gated by examining the fluid pressure and velocity fields, the bubble dynamics,  
and the transient structural deformation and stresses.

It is found that as  $p_0$  varies, the final configuration of the cylinder can be  
690 substantially different. Results from five representative cases ( $p_0 = 8$  MPa,  
12.5 MPa, 25 MPa, 50 MPa, 100 MPa) are discussed in detail. In these cases,  
the structural dynamics varies from a cyclic elastic vibration without collapse  
( $p_0 = 8$  MPa) to an immediate collapse without vibration ( $p_0 = 100$  MPa).  
Three different types of collapse behaviors are observed, which are categorized  
695 as Mode 2A, Mode 2B, and Mode 2C (Figure 20). As  $p_0$  increases, the mode of  
collapse changes from 2A to 2B, and then from 2B to 2C. The mode transitions  
are discussed using additional test cases in the parametric study.

The mechanisms of the three collapse modes are summarized below. Mode  
2A is caused by a coincidence between the bubble's first contraction phase and  
700 the cylinder's horizontal compression. As the bubble contracts, it emits a pres-  
sure pulse that elevates the pressure around the entire cylinder. When this  
bubble pulse arrives at the horizontally compressed cylinder, it facilitates its  
compression, leading to an horizontal collapse that has been observed earlier in  
a laboratory experiment [5]. Mode 2B is related to the plastic deformation in-  
705 duced by the initial loads, i.e., the initial shock wave and the water flow caused  
by the bubble's initial expansion. This plastic deformation suppresses the verti-  
cal extension and horizontal compression of the cylinder. As a result, when the  
aforementioned bubble pulse arrives at the cylinder, the cylinder is compressed  
in vertical direction. The bubble pulse facilitates this compression, leading to  
710 collapse mode 2B. For Mode 2C collapse, the result suggests that the cylin-

der's collapse is directly induced by the incident shock wave from the explosion. Clearly, the dynamics of the explosion bubble has a significant effect in collapse Modes 2A and 2B. In both cases, the plastic deformation remains relatively small long after the initial loads have passed. The collapse of the cylinder starts  
715 only after the bubble contracts to its first minimum size and emits a pressure pulse.

The time that the cylinder takes to completely collapse does not decrease monotonically as  $p_0$  increases (cf. Figure 21). When the cylinder collapses in Mode 2A, increasing  $p_0$  may cause the cylinder to take more time to reach  
720 self-contact. This phenomenon is caused by the increased amount of plastic deformation induced by the initial loads from the explosion.

The simulation result also reveals that the dynamics of an explosion bubble near a vibrating or collapsing cylinder is significantly different from the dynamics of bubbles in free field or near a rigid wall. In other words, the transient  
725 structural deformation has a clear effect on the bubble dynamics. In particular, in the cases with  $p_0 \geq 8$  MPa, a counter-jet that points away from the structural surface is observed. The formation of this counter-jet is induced by the vibration and collapse of the cylinder. This type of phenomenon has been observed previously in bubbles expanding near an elastic solid body. Compared to the  
730 liquid jets produced by bubbles collapsing near a rigid wall, this counter-jet is in the opposite direction.

### **Declaration of competing interest**

The authors have no relevant financial or non-financial competing interests.

### **Acknowledgement**

735 W.M., X.Z., and K.W. gratefully acknowledge the support of the Office of Naval Research (ONR) under Awards N00014-19-1-2102, and the support of the National Science Foundation (NSF) under Awards CBET-1751487. C.G.

gratefully acknowledges ONR N00014-10-C-0108 and Prof. James H. Duncan from the University of Maryland.

740 **References**

- [1] R. Cole, Underwater explosions, Princeton University Press, 1948.
- [2] M. M. Swisdak Jr, Explosion effects and properties. part ii. explosion effects in water, Tech. rep., Naval Surface Weapons Center White Oak Lab, Silver Spring, MD (1978).
- 745 [3] Z. Liu, Y. L. Young, Transient response of submerged plates subject to underwater shock loading: an analytical perspective, *Journal of applied mechanics* 75 (4) (2008).
- [4] A. K. Mathew, Modeling underwater explosion (undex) shock effects for vulnerability assessment in early stage ship design, Master's thesis, Virginia  
750 Tech (2018).
- [5] C. Ikeda, Fluid-structure interactions: implosions of shell structures and wave impact on a flat plate, Ph.D. thesis, University of Maryland, College Park (2012).
- [6] S. Gupta, H. Matos, J. M. LeBlanc, A. Shukla, Shock initiated instabilities  
755 in underwater cylindrical structures, *Journal of the Mechanics and Physics of Solids* 95 (2016) 188–212.
- [7] J. LeBlanc, C. Shillings, E. Gauch, F. Livolsi, A. Shukla, Near field underwater explosion response of polyurea coated composite plates, *Experimental Mechanics* 56 (4) (2016) 569–581.
- 760 [8] E. L. Guzas, S. Gupta, J. M. Ambrico, J. M. LeBlanc, A. Shukla, Computational modeling of dynamically initiated instabilities and implosion of underwater cylindrical structures in a confined environment, *Journal of Applied Mechanics* 86 (2) (2019).

- [9] W. Ma, X. Zhao, K. Wang, A fluid-structure coupled computational model  
765 for the certification of shock-resistant elastomer coatings, in: Proceedings of 39th International Conference on Offshore Mechanics and Arctic Engineering, Vol. 2A: Structures, Safety, and Reliability, ASME, 2020, v02AT02A024.
- [10] C. Javier, M. Galuska, M. Papa, J. LeBlanc, H. Matos, A. Shukla, Under-  
770 water explosive bubble interaction with an adjacent submerged structure, Journal of Fluids and Structures 100 (2021) 103189.
- [11] S. Kyriakides, E. Corona, Mechanics of offshore pipelines: volume 1 buck-  
ling and collapse, Vol. 1, Elsevier, 2007.
- [12] C. Ikeda, J. Wilkerling, J. Duncan, The implosion of cylindrical shell struc-  
775 tures in a high-pressure water environment, Proceedings of the Royal Society A: Mathematical, Physical and Engineering Sciences 469 (2160) (2013) 20130443.
- [13] C. Farhat, K. Wang, A. Main, S. Kyriakides, L.-H. Lee, K. Ravi-Chandar,  
780 T. Belytschko, Dynamic implosion of underwater cylindrical shells: experiments and computations, International Journal of Solids and Structures 50 (19) (2013) 2943–2961.
- [14] S. E. Turner, J. M. Ambrico, Underwater implosion of cylindrical metal  
tubes, Journal of Applied Mechanics 80 (1) (2013).
- [15] S. Kishore, P. N. Parrikar, N. DeNardo, A. Shukla, Underwater dynamic  
785 collapse of sandwich composite structures, Experimental Mechanics 59 (5) (2019) 583–598.
- [16] S. Cao, G. Wang, O. Coutier-Delgosha, K. Wang, Shock-induced bubble  
collapse near solid materials: effect of acoustic impedance, Journal of Fluid  
Mechanics 907 (2021) A17.

- 790 [17] D. Gibson, Cavitation adjacent to plane boundaries, in: Proceedings of  
3rd Australasian Conference on Hydraulics and Fluid Mechanics, Sydney,  
Australia, 1968, pp. 210–214.
- [18] D. Gibson, J. Blake, Growth and collapse of cavitation bubbles near flexible  
boundaries, in: Proceedings of 7th Australasian Conference on Hydraulics  
795 and Fluid Mechanics, Brisbane, Australia, 1980, pp. 283–286.
- [19] J. R. Blake, D. C. Gibson, Cavitation bubbles near boundaries, *Annual  
Review of Fluid Mechanics* 19 (1) (1987) 99–123.
- [20] J. H. Duncan, S. Zhang, On the interaction of a collapsing cavity and a  
compliant wall, *Journal of Fluid Mechanics* 226 (1991) 401–423.
- 800 [21] S. Li, A.-M. Zhang, R. Han, Letter: Counter-jet formation of an expanding  
bubble near a curved elastic boundary, *Physics of Fluids* 30 (12) (2018)  
121703.
- [22] K. G. Wang, P. Lea, C. Farhat, A computational framework for the sim-  
ulation of high-speed multi-material fluid–structure interaction problems  
with dynamic fracture, *International Journal for Numerical Methods in*  
805 *Engineering* 104 (7) (2015) 585–623.
- [23] K. Wang, A. Rallu, J.-F. Gerbeau, C. Farhat, Algorithms for interface  
treatment and load computation in embedded boundary methods for fluid  
and fluid-structure interaction problems, *International Journal for Numer-  
ical Methods in Fluids* 67 (9) (2011) 1175–1206.  
810
- [24] C. Farhat, J.-F. Gerbeau, A. Rallu, Fiver: A finite volume method based  
on exact two-phase riemann problems and sparse grids for multi-material  
flows with large density jumps, *Journal of Computational Physics* 231 (19)  
(2012) 6360–6379.
- 815 [25] A. Main, X. Zeng, P. Avery, C. Farhat, An enhanced FIVER method for  
multi-material flow problems with second-order convergence rate, *Journal  
of Computational Physics* 329 (2017) 141–172.

- [26] D. Z. Huang, D. De Santis, C. Farhat, A family of position- and orientation-independent embedded boundary methods for viscous flow and fluid–structure interaction problems, *Journal of Computational Physics* 365 (2018) 74–104.
- [27] C. Farhat, A. Rallu, K. Wang, T. Belytschko, Robust and provably second-order explicit–explicit and implicit–explicit staggered time-integrators for highly non-linear compressible fluid–structure interaction problems, *International Journal for Numerical Methods in Engineering* 84 (1) (2010) 73–107.
- [28] K. Wang, J. Gretarsson, A. Main, C. Farhat, Computational algorithms for tracking dynamic fluid–structure interfaces in embedded boundary methods, *International Journal for Numerical Methods in Fluids* 70 (2012) 515–535.
- [29] C. Farhat, A. Rallu, S. Shankaran, A higher-order generalized ghost fluid method for the poor for the three-dimensional two-phase flow computation of underwater implosions, *Journal of Computational Physics* 227 (16) (2008) 7674–7700.
- [30] K. G. Wang, Multiphase fluid-solid coupled analysis of shock-bubble-stone interaction in shockwave lithotripsy, *International journal for numerical methods in biomedical engineering* 33 (10) (2017) e2855.
- [31] S. Cao, Y. Zhang, D. Liao, P. Zhong, K. G. Wang, Shock-induced damage and dynamic fracture in cylindrical bodies submerged in liquid, *International journal of solids and structures* 169 (2019) 55–71.
- [32] G. Xiang, X. Ma, C. Liang, H. Yu, D. Liao, G. Sankin, S. Cao, K. Wang, P. Zhong, Variations of stress field and stone fracture produced at different lateral locations in a shockwave lithotripter field, *The Journal of the Acoustical Society of America* 150 (2) (2021) 1013–1029.

- 845 [33] C. Leblond, J.-F. Sigrist, A versatile approach to the study of the transient response of a submerged thin shell, *Journal of Sound and Vibration* 329 (1) (2010) 56–71.
- [34] S. Iakovlev, Interaction between a submerged evacuated cylindrical shell and a shock wave—part i: Diffraction–radiation analysis, *Journal of Fluids and Structures* 24 (7) (2008) 1077–1097.
- 850 [35] S. Iakovlev, Interaction between a submerged evacuated cylindrical shell and a shock wave—part ii: Numerical aspects of the solution, *Journal of Fluids and Structures* 24 (7) (2008) 1098–1119.
- [36] S. Iakovlev, Interaction between an external shock wave and a cylindrical shell filled with and submerged into different fluids, *Journal of Sound and Vibration* 322 (1) (2009) 401–437.
- 855 [37] S. Cao, A. Main, K. G. Wang, Robin-neumann transmission conditions for fluid-structure coupling: Embedded boundary implementation and parameter analysis, *International Journal for Numerical Methods in Engineering* 115 (5) (2018) 578–603.
- 860 [38] B. van Leer, Towards the ultimate conservative difference scheme. v. a second-order sequel to godunov’s method, *Journal of Computational Physics* 32 (1) (1979) 101–136.
- [39] P. Roe, Approximate riemann solvers, parameter vectors, and difference schemes, *Journal of Computational Physics* 43 (2) (1981) 357–372.
- 865 [40] A. Main, C. Farhat, A second-order time-accurate implicit finite volume method with exact two-phase riemann problems for compressible multi-phase fluid and fluid–structure problems, *Journal of Computational Physics* 258 (2014) 613–633.
- 870 [41] K. G. Wang, P. Lea, A. Main, O. McGarity, C. Farhat, Predictive simulation of underwater implosion: coupling multi-material compressible fluids



with cracking structures, in: Proceedings of 33rd International Conference on Offshore Mechanics and Arctic Engineering, Vol. 8A: Ocean Engineering, ASME, 2014, v08AT06A028.

- 875 [42] K. G. Wang, Multiphase fluid-solid coupled analysis of shock-bubble-stone interaction in shockwave lithotripsy, *International Journal for Numerical Methods in Biomedical Engineering* 33 (10) (2017) e2855.
- [43] S. Gupta, J. M. LeBlanc, A. Shukla, Mechanics of the implosion of cylindrical shells in a confining tube, *International Journal of Solids and Structures* 880 51 (23) (2014) 3996–4014.
- [44] T. Muttaqie, S. Hyun Park, J. Min Sohn, S.-R. Cho, I. Sik Nho, S. Han, P.-S. Lee, Y. Sik Cho, Experimental investigations on the implosion characteristics of thin cylindrical aluminium-alloy tubes, *International Journal of Solids and Structures* 200-201 (2020) 64–82.
- 885 [45] C. J. Salazar, A. Shukla, Hydrostatic implosion of composite cylinders in an open-ended confining structure, *Composites Part B: Engineering* 192 (2020) 107993.
- [46] Y. Kwon, P. Fox, Underwater shock response of a cylinder subjected to a side-on explosion, *Computers & Structures* 48 (4) (1993) 637–646.
- 890 [47] R. Blevins, *Formulas for natural frequency and mode shape*, Van Nostrand Reinhold Company, 1979.
- [48] C. K. Turangan, G. J. Ball, A. R. Jamaluddin, T. G. Leighton, Numerical studies of cavitation erosion on an elastic-plastic material caused by shock-induced bubble collapse, *Proceedings of the Royal Society A: Mathematical, Physical and Engineering Sciences* 473 (2205) (2017) 20170315.
- 895 [49] L. T. Liu, X. L. Yao, A. M. Zhang, Y. Y. Chen, Numerical analysis of the jet stage of bubble near a solid wall using a front tracking method, *Physics of Fluids* 29 (1) (2017) 012105.

- [50] E.-A. Brujan, T. Noda, A. Ishigami, T. Ogasawara, H. Takahira, Dynamics of laser-induced cavitation bubbles near two perpendicular rigid walls, *Journal of Fluid Mechanics* 841 (2018) 28–49.
- [51] C. E. Brennen, *Cavitation and bubble dynamics*, Cambridge University Press, 2013.